

**FIRE RESISTANCE AND DESIGN OF COMPOSITE COLUMNS AND  
WALLS**

by

**Preshit Wazalwar**

**A Thesis**

*Submitted to the Faculty of Purdue University*

*In Partial Fulfillment of the Requirements for the degree of*

**Master of Science in Civil Engineering**



Lyles School of Civil Engineering

West Lafayette, Indiana

May 2020

**THE PURDUE UNIVERSITY GRADUATE SCHOOL**  
**STATEMENT OF COMMITTEE APPROVAL**

**Dr. Amit H. Varma, Chair**

Lyles School of Civil Engineering

**Dr. Arun Prakash**

Lyles School of Civil Engineering

**Dr. Garrett D. Jeong**

Lyles School of Civil Engineering

**Approved by:**

Dr. Dulcy M. Abraham

*Dedicated to my family*

## **ACKNOWLEDGMENTS**

I would like to start by thanking my advisor, Dr. Amit H. Varma for providing me the opportunity to work on this project, and for his constant guidance, motivation and positive attitude throughout my work. I would also like to thank Dr. Saahastranshu R. Bhardwaj, for being a part of the project and for providing me with help and direction throughout my study. I also thank him for all the valuable inputs and suggestions he provided to shape my research. Further, I would like to thank Ataollah Taghipour Anvari for his contribution to the project. I would like to extend my gratitude to the members of my examining committee, Dr. Arun Prakash and Dr. Garrett D. Jeong for their time, guidance and support.

The project is funded by Charles Pankow Foundation, Steel Institute of New York (SINY), and American Institute of Steel Construction (AISC). The author is grateful to these agencies for financial support and would also like to thank them for their continued support.

I would like to express my gratitude and love to my parents, family and friends for their supports and encouragements.

## TABLE OF CONTENTS

LIST OF TABLES .....	7
LIST OF FIGURES .....	8
ABSTRACT .....	11
1. INTRODUCTION .....	12
1.1. Background of Composite Axial Members.....	12
1.2. Fire Loading: Axial Members .....	13
1.3. Research Scope and Objectives .....	13
1.4. Research Plan and Thesis Outline .....	14
2. BACKGROUND .....	16
2.1. Prior Experimental Research on CFTs and C-PSWs at Elevated Temperatures.....	16
2.2. Prior Numerical Research on CFTs and C-PSWs at Elevated Temperatures .....	17
2.3. Material Models at Elevated Temperatures.....	18
2.3.1. Lie’s Stress-Strain models for concrete (1992) .....	18
2.3.2. Lie’s Stress-Strain model for steel (1995).....	18
2.3.3. Poh’s Stress-Strain model for steel (2001).....	18
2.3.4. Eurocode proposed stress-strain curves (2005).....	18
3. 2D NUMERICAL MODEL- DEVELOPMENT AND BENCHMARKING .....	23
3.1. Model Algorithm and Working .....	23
3.1.1. 2D Heat Transfer Analysis .....	23
3.1.2. Section Moment-Curvature Analysis.....	24
3.1.3. Non-linear Column Buckling Analysis.....	25
3.2. Material Stress-strain-temperature Models .....	26
3.3. Fiber-Model Validation and Benchmarking.....	27
3.3.1. Ambient Temperatures.....	27
3.3.2. Elevated Temperatures.....	28
3.4. Limitations of the fiber model.....	30
3.5. Development and Functioning of User Interface.....	31
3.5.1. Pre-Processor .....	31
3.5.2. Post-Processor- .....	31

4.	CFT PARAMETRIC STUDY AND CAPACITY PREDICTION.....	44
4.1.	Parametric Studies .....	44
4.1.1.	Section Aspect Ratio.....	45
4.1.2.	Cross Section Slenderness.....	45
4.1.3.	Steel Yield Strength .....	46
4.1.4.	Concrete Compressive Strength .....	46
4.2.	Effect of Fire Protection.....	46
4.3.	Concrete Contribution Factor to Stiffness.....	47
4.4.	Capacity Prediction Equation for CFTs at Elevated Temperature .....	49
5.	C-PSW/CF MODELING AND ANALYSIS .....	60
5.1.	Section-based Models .....	60
5.2.	Strip-based Models .....	62
5.3.	Single-sided Heating: Strip-based Approach .....	64
6.	SUMMARY AND CONCLUSIONS .....	80
	REFERENCES .....	82

## LIST OF TABLES

Table 3.1: Comparison of experimental, fiber-model predicted and AISC 2016 predicted compressive strengths at ambient temperature .....	32
Table 3.2: Comparison of failure surface temperature for 6 wall specimens from FE analysis and fiber-model .....	32
Table 3.3: Various combinations of material models tested .....	32
Table 4.1: Parametric study matrix for CFTs at elevated temperature.....	52
Table 5.1: Details of wall specimens for comparison with FE analysis.....	67
Table 5.2: Comparison of failure time and surface temperature as predicted by fiber model and FE analysis .....	67

## LIST OF FIGURES

Figure 2.1: (a): Concrete stress-strain curves at elevated temperatures developed by Lie (1992). Ref: Hong (2007); (b): Steel stress-strain curves at elevated temperatures developed by Lie and Irwin (1995). Ref: Hong (2007).....	20
Figure 2.2: Stress-strain curves for 330 MPa steel developed using Poh’s model. Ref: Hong (2007) .....	21
Figure 2.3: Eurocode stress-strain-temperature curves for 420 MPa steel.....	21
Figure 2.4: Eurocode stress-strain-temperature curves for 40 MPa concrete .....	22
Figure 3.1: Representation of CFT section discretized into fibres .....	33
Figure 3.2: Representation if the three modes of heat transfer: convection, conduction & radiation .....	33
Figure 3.3: Schematic flowchart of algorithm for 2D heat transfer.....	34
Figure 3.4: Flowchart showing the algorithm to generate Moment-Curvature Plot.....	34
Figure 3.5: Flowchart showing the algorithm of Newmark’s Inelastic Column Buckling Analysis .....	35
Figure 3.6: (a) Effective stress-strain curves for compact ( $\lambda=50$ ), non-compact ( $\lambda=67$ ) and slender( $\lambda=100$ ) sections for steel ( $F_y=358$ MPa) at ambient temperature; (b) Effective stress-strain curves for 330 MPa steel at elevated temperatures.....	36
Figure 3.7: Representative validation of the Fiber Model carried out by Hong. Ref: Hong (2007) .....	37
Figure 3.8: Comparison of compressive strength (load vs. lateral displacement) for (a) conventional (elastic-perfectly-plastic) and (b) effective (Lai et al. 2016) steel models versus AISC (2016) predicted strength.....	37
Figure 3.9: (a) Temperature profiles across the section at various time instants; Comparison of fiber model predicted and FEM data; (b) Surface temperature vs time for 3-sided heating: comparison of experimental data and fiber model. The plot shows the temperature of a point on the un-heated surface.....	38
Figure 3.10: Comparison of steel surface temperature at failure as predicted by the fiber-model and FE analysis for C-PSWs .....	39
Figure 3.11: (a) Axial displacement vs time and (b) Axial displacement vs temperature for the wall specimen for different combinations of material models, plotted with the FE analysis obtained curve; The curves are labelled by the steel and concrete model respectively .....	40

Figure 3.12: (a) Axial displacement vs time and (b) Axial displacement vs temperature for the CFT specimen for different combinations of material models, plotted with the FE analysis obtained curve; The curves are labelled by the steel and concrete model respectively .....	41
Figure 3.13: (a) Pre-processor interface of the UI, with all input variables (b) Advanced options interface of the UI .....	42
Figure 3.14: Examples of post-processor output interfaces .....	43
Figure 4.1: Critical load versus slenderness at two surface temperatures for various aspect ratios .....	53
Figure 4.2: Critical load versus slenderness curves at two surface temperatures for varying section slenderness (reinforcement ratio).....	53
Figure 4.3: Critical load versus slenderness curves at two surface temperatures for varying steel yield strength .....	54
Figure 4.4: Critical load versus slenderness curves at two surface temperatures for varying concrete compressive strength.....	54
Figure 4.5: Critical load vs Slenderness comparison for two steel surface temperatures for a column with and without fire protection.....	55
Figure 4.6: Temperature profiles for a column at failure with and without fire protection for steel surface temperature = 600 °C .....	55
Figure 4.7: (a) Axial displacement vs surface temperature and (b) axial displacement vs time comparisons for a column with and without fire protection.....	56
Figure 4.8: Variation of concrete contribution factor to stiffness (C3) with section slenderness and axial load for (a) aspect ratio = 1 & column slenderness = 5, (b) aspect ratio = 1 & column slenderness = 15, (c) aspect ratio = 2 & column slenderness = 5, (d) aspect ratio = 2 & column slenderness = 15.....	57
Figure 4.9: Normalized results of the parametric studies plotted with the proposed theoretical capacity curves (lower-bound, median and simplified bi-linear) .....	59
Figure 5.1: Normalized results of the comparison between fiber-model and FEM data for wall specimens using section method for (a) 200 mm wall thickness and (b) 300 mm wall thickness	68
Figure 5.2: Comparison of fiber-model and FE analysis predicted axial displacements for CW-200 specimens using section method; (a) axial displacement vs time and (b) axial displacement vs surface temperature .....	69
Figure 5.3: Comparison of fiber-model and FE analysis predicted axial displacements for CW-300 specimens using section method; (a) axial displacement vs time and (b) axial displacement vs surface temperature .....	70

Figure 5.4: Schematic of a wall section for strip-based modeling approach .....	71
Figure 5.5: Temperature profiles comparison at three time instants for half section (CW-200) between fiber model and finite element model- strip method .....	71
Figure 5.6: Comparison of failure surface temperatures as predicted by fiber model and FE analysis- strip method .....	72
Figure 5.7: Comparison of axial displacements for (a) CW-200 specimens and (b) CW-300 specimens using strip method .....	73
Figure 5.8: Normalized results of the comparison between fiber-model and FEM data for (a) CW-200 specimens and (b) CW-300 & CW-400 specimens using strip method .....	74
Figure 5.9: Comparison of normalized load vs slenderness data for section method and strip method for fiber-model .....	75
Figure 5.10: Comparison of cross-section temperature profiles at three time instants (CW-300) for fiber model and FEM for single-sided heating .....	75
Figure 5.11: Comparison of fiber model and FE analysis predicted out-of-plane displacement against temperature for single-sided heating of the exposed steel surface for CW-300-10 specimen .....	76
Figure 5.12: Out-of-plane displacement against temperature of the exposed steel surface for 6 slenderness (L/d) ratios for CW-300-xx-20 wall section for single-sided heating .....	76
Figure 5.13: Representation of the two types of moments generated in a wall section exposed to asymmetric heating .....	77
Figure 5.14: (a) Failure surface temperature and (b) Failure time vs applied axial load ratio for slenderness = 25 (CW-300-25) for single-sided heating .....	78
Figure 5.15: Variation of time to failure (fire resistance) with wall slenderness (single-sided heating) for applied axial load equal to 20% and 30% $A_g f_c$ for CW-300 specimens .....	79
Figure 5.16: Normalized critical load vs slenderness data points for single-sided heating .....	79

## ABSTRACT

Composite axial members [Concrete-filled Steel Tube (CFT) columns and Composite-Plate Shear Walls/Concrete Filled (C-PSWs/CF)] may be subjected to a combination of loading conditions, such as gravity, wind, seismic or fire. Under fire loading, the member would experience degradation of material properties and non-uniform temperature distribution through the cross-section. A time-temperature study is necessary to determine the member capacity and stability under fire loading.

This thesis presents (a) the development and validation of a 2D fiber-based numerical analysis tool for modeling composite axial members under fire loading and (b) the results of benchmarked numerical studies conducted on composite axial members (CFTs and C-PSWs). The studies involved simulating fire conditions by exposing steel faceplates to elevated temperatures (ASTM E119 Time-Temperature Curve) while maintaining a constant axial load. The fiber model was benchmarked using experimental results and further validated with benchmarked Finite Element (FE) models.

The parametric study on CFTs involved analyzing the effect column slenderness, column aspect ratio, section slenderness, and material properties on the behavior of columns at elevated temperatures. Section slenderness and concrete strength were seen to have a significant effect on column capacity, while aspect ratio and steel yield strength had a minor influence. A layer of fire protection was modeled to understand its effect on stability (failure time and critical load). It was observed that a layer of fire protection delayed the time to failure (Fire Rating) but caused the member to fail at marginally lower axial loads. The parametric study results are used to develop equations for calculating the compression strength of CFTs at elevated temperatures.

The studies on C-PSWs involved modeling the walls using two methods, which are analyzing the entire wall section and analyzing a strip of the wall section. Results from both methods are compared with finite-element and experimental data and proposed equations for axial capacity are validated. One-sided heating of walls is also explored and validated.

# 1. INTRODUCTION

## 1.1. Background of Composite Axial Members

Composite axial members consist of Concrete Filled Steel Tube (CFT) columns and Composite-Plate Shear Walls/Concrete filled (C-PSW/CF). CFT columns are typically made up of rectangular or circular hollow structural sections (HSS or steel tubes) filled with concrete. These columns are popular in construction as they combine the structural properties and advantages of steel and concrete. The steel tube acts as formwork and provides confinement to the concrete infill, thus improving the performance of concrete and cutting down the need to erect and demolish separate formwork. The concrete infill acts as a lateral support to the steel tube, delaying the local buckling of the steel tubes.

C-PSWs consist of two steel faceplates running along the length of the wall filled with concrete, which together acts as the web of the structure. These walls are typically reinforced by boundary elements towards their ends which act as flanges. The steel web faceplates are held in place using tie bars connecting them. Steel headed stud anchors (shear studs) are welded to them to provide composite action with concrete. C-PSWs provide similar advantages to CFTs, which are faster construction and improved material performance.

Extensive studies have been conducted to evaluate the ambient behavior of composite members, under various combinations of axial, bi-axial and seismic loading. A number of researchers have compiled databases for experimental data on square, rectangular and circular composite columns (Lue et al., 2006). The current AISC Steel Specification (AISC, 2016) provides design equations for composite structures (encased and filled) under axial, flexural and combined loading (AISC 360, Chapter I). Experimental and numerical research has also been conducted on C-PSWs under various loading combinations to develop numerical models and propose design equations (Sener and Varma, 2014; Bhardwaj et al., 2019a). However, these models cannot be extrapolated to elevated temperatures because of two main reasons: (i) temperature-dependent degradation of material properties at high temperatures and (ii) temperature gradient across the CFT section.

## **1.2. Fire Loading: Axial Members**

Structures can be occasionally subjected to extreme loading events such as fire loading. In the case of a fire event, a structural column or wall may be exposed to elevated temperatures on all or some of its sides. These elevated temperatures cause a degradation of both strength and stiffness of the material. A column carrying a constant axial load can thus fail when exposed to persistent heating. Composite members typically have a better fire resistance as compared to conventional steel members, due to the low thermal conductivity of concrete. When exposed to fire, CFTs and C-PSWs develop a temperature gradient across the section, with the concrete core being at significantly lower temperatures. Hence, most of the load is resisted by the core concrete.

Experimental studies of composite axial members using standard (ASTM E119) fire curves (ASTM, 2003) have been carried out and empirical equations have been proposed to predict their fire rating and capacity (Kodur and Mackinnon, 2000; Lie et al., 1995). Numerical studies conducted on CFTs have focused on developing and benchmarking of 3D finite-element models to understand the fundamental behavior of CFTs under fire loading.

The current AISC Steel Specification (AISC 360, 2016: Appendix A4) provides equations to predict axial and flexural capacity for steel members at elevated temperatures. For composite members, a prescriptive approach is recommended which is based on empirical equations derived by researchers. While the current building code allows for performance-based design, it is not very common. The prescriptive approach involves using standard shapes and sections to attain a target fire resistance rating (FRR), which is defined as the time (in hours) to failure under standard (ASTM E119) fire loading (ASTM, 2003). The FRR values can also be obtained experimentally, which require standard fire tests of the designed members.

## **1.3. Research Scope and Objectives**

There are currently no provisions to obtain the capacity of composite axial or flexural members under fire loading. Additionally, the equations proposed in literature are primarily empirical i.e. based only on the experimental results obtained by the researchers. As a result, they cannot be extended to generalized fire scenarios or structural designs other than those that were tested. This results in a prescriptive design approach of composite structures under fire loading and limits innovation and optimization.

There is thus a need for performance-based design methodologies for composite members which would allow a more diverse range of structures to be designed using composites. Additionally, there is a need for simplistic analytical models based on fundamental principles of mechanics that can predict the behavior of a broad category of structures under standard as well as user-defined fire loading scenarios. These tools will further aid in performance-based design of composite structures and permit a greater scope for optimization and innovation.

There are three main objectives of this research, they are:

- (i) Develop a performance-based analysis tool for composite axial members under fire loading. The tool would be based on fundamental principles of mechanics and thus would be applicable in all scenarios.
- (ii) Conduct a parametric study on CFT columns, to study and quantify the effect of various parameters on CFT stability. An equation to estimate column capacity would also be proposed based on the results
- (iii) Analyze C-PSWs/CF by two methods: as a whole section and as discrete strips; compare the analysis results to experimental and finite-element data and validate the design equations proposed for C-PSWs

#### **1.4. Research Plan and Thesis Outline**

As the first step of the study, a 2D fiber-based analysis tool was developed to carry out the analyses, which was validated and benchmarked using experimental data and 3D Finite-Element (FE) analysis results. A user interface was also developed to allow easy interaction. This development and validation of the fiber model is presented in detail in 3.

This fiber model was then used to conduct a parametric study on CFTs, which included studying the effect of fire protection strategies. The results of this study were combined into design equations to predict the axial load capacity for CFTs. The details of the parametric study, their results and proposed equations are discussed in 4. Next, the fiber model was used to model C-PSW/CF specimens using the section-based and the strip-based approaches mentioned in the previous section. The obtained results were compared to finite-element models and experimental data. The results from the fiber model were also used to validate the design equations proposed for C-PSWs. Single-sided heating of 2D wall sections was modeled using the strip-based approach.

Obtained results were compared with FE analysis results and a preliminary study was conducted to analyze the effect of wall slenderness on stability. These analyses and results are covered in 5.

## 2. BACKGROUND

### 2.1. Prior Experimental Research on CFTs and C-PSWs at Elevated Temperatures

Several experimental studies have been conducted on composite members exposed to fire loading. These studies have focused on understanding different aspects of the fundamental behavior of composite members under fire loading. The experimental studies involved heating a CFT specimen in a furnace, the gas temperature of which was controlled to follow the standard time-temperature curve as specified in ASTM E119 (ASTM, 2003). A constant or varying axial or lateral load was applied. These studies mainly focused on understanding the material properties and fire resistance ratings.

Lie et al. (1995) tested three specimens of hollow structural steel filled with bar-reinforced concrete. Material models for steel and concrete at elevated temperatures were developed based on the results. An analytical approach was also proposed to calculate the axial capacity of reinforced square CFT members under uniform (symmetric) fire conditions. Poh (2001) used experimental data from several tests to propose a new stress-strain-temperature relationship for structural steel. This material model is further discussed in the next section.

Kodur and Mackinnon (2000) used data from 58 tests on plain, bar-reinforced and fiber-reinforced CFTs to develop empirical equations for prediction of fire resistance ratings. Empirical design equations were also proposed based on the tests and parametric studies. Yang et al. (2013) tested six full-scale square CFT specimens under non-uniform fire (one-sided and three-sided). They characterized various parameters influencing the performance of CFTs and also developed 3D numerical models for simulating the same. Wei et al. (2017) tested 12 C-PSW specimens under uniform and non-uniform fire loading. They varied several parameters (such as wall thickness, steel ratio, tie-bar spacing) and proposed preliminary design recommendations based on their observations.

These experimental studies conducted mainly focused on simulating fire scenarios as specified by the design codes for composite members, thus the empirical equations so developed are applicable only to limited design cases.

## 2.2. Prior Numerical Research on CFTs and C-PSWs at Elevated Temperatures

Several analytical and numerical studies have been conducted on composite members under fire loading. These studies have focused on developing accurate 3D models that are benchmarked based on experimental data.

Hong et al. (2008) developed a 3D Finite Element (FE) model using ABAQUS to study the behavior of CFTs under fire loading. The models were benchmarked using experimental data and were used to predict CFT response at elevated temperatures. Detailed development and benchmarking of these models is given in Hong et al. (2008) and Hong (2007). Lie (1995) had proposed an analytical approach to calculate the axial capacity of reinforced square CFTs. (Heinisuo and Jokinen 2014) developed 3D Finite-Element models to simulate non-symmetric heating of square CFT columns. Fischer and Varma (2015) developed a 3D FE model for composite beams and their connections subjected to gravity and fire loads. The models were used to provide additional insight into the axial forces developed in the connections, particularly during the cooling phase. Bhardwaj et al. (2019) have developed and benchmarked a 3D FE model for C-PSWs under fire loading. 3D finite-element models have a high level of detail and are computationally expensive. As a result, it may be difficult to use them in conventional design scenarios.

2D fiber-based models of CFTs exposed to fire loading have been developed by Hong et al. (2009), which are simplified compared to 3D FE models. The simplifying assumptions include that the temperature along the length of the member is assumed to be constant, thus heat transfer is performed only in 2D (across the section). Additionally, local buckling effects of steel faceplates are ignored. Detailed development and validation of the model is given in Hong (2007) and Hong et al. (2009). This model was found to be reasonably accurate in predicting key parameters of CFT behavior, when compared to experimental and finite-element data (Hong et al. 2009). 2D fiber-based models have the advantage of being computationally economical. However, the 2D model developed by Hong et al. (2009) has a very limited applicability (only applicable to square CFTs with uniform faceplate thickness and all-sided fire) and thus cannot be effectively used for all fire loading scenarios. This fiber model was used as the starting point for the current study, and the author built upon it to develop a more generic model having a wider applicability.

### 2.3. Material Models at Elevated Temperatures

Material stress-strain relationships at elevated temperatures are complex and difficult to model accurately. However, several researchers have developed simplified stress-strain-temperature models for steel and concrete based on experimental studies. Several of the relevant material models used in this study are discussed here.

#### 2.3.1. *Lie's Stress-Strain models for concrete (1992)*

Lie (1992) developed a mathematical stress-strain relationship for confined concrete at elevated temperatures. Lie's expression assumes that concrete compressive strength remains constant from 20°C to 400°C but the elastic modulus falls to about 40% or 50% of the original value. After 400°C, concrete both compressive strength and elastic modulus decrease. This model ignores any strength of concrete in tension. The equations for the material model are given in Lie (1992) and the stress-strain curves at various temperatures are shown in Figure 2.1(a).

#### 2.3.2. *Lie's Stress-Strain model for steel (1995)*

Lie and Irwin (1995) proposed a mathematical stress-strain relationship for steel at elevated temperatures based on the results of tests on CFTs under fire loading. This model for steel is symmetric in tension and compression. Softening and strength reduction at elevated temperature is accounted for by reducing Young's modulus and yield strength with temperature. The equations for the material model are given in Lie (1992) and the stress-strain curves at various temperatures are shown in Figure 2.1(b).

#### 2.3.3. *Poh's Stress-Strain model for steel (2001)*

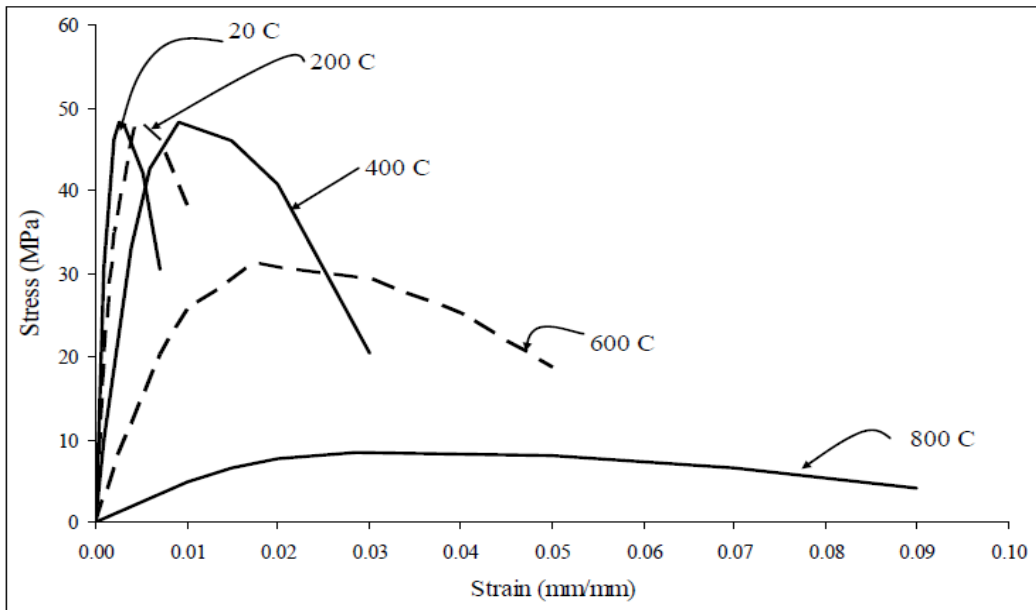
Poh (2001) proposed a mathematical relationship for the stress-strain-temperature ( $\sigma$ - $\varepsilon$ - $T$ ) behavior of structural steel. Poh (2001) based his equations on experimental results of stress-strain ( $\sigma$ - $\varepsilon$ ) responses of conventional steel at elevated temperatures. The experimental background and development of equations is covered in Poh (2001) and Figure 2.2 presents the stress-strain curves at different temperatures.

#### 2.3.4. *Eurocode proposed stress-strain curves (2005)*

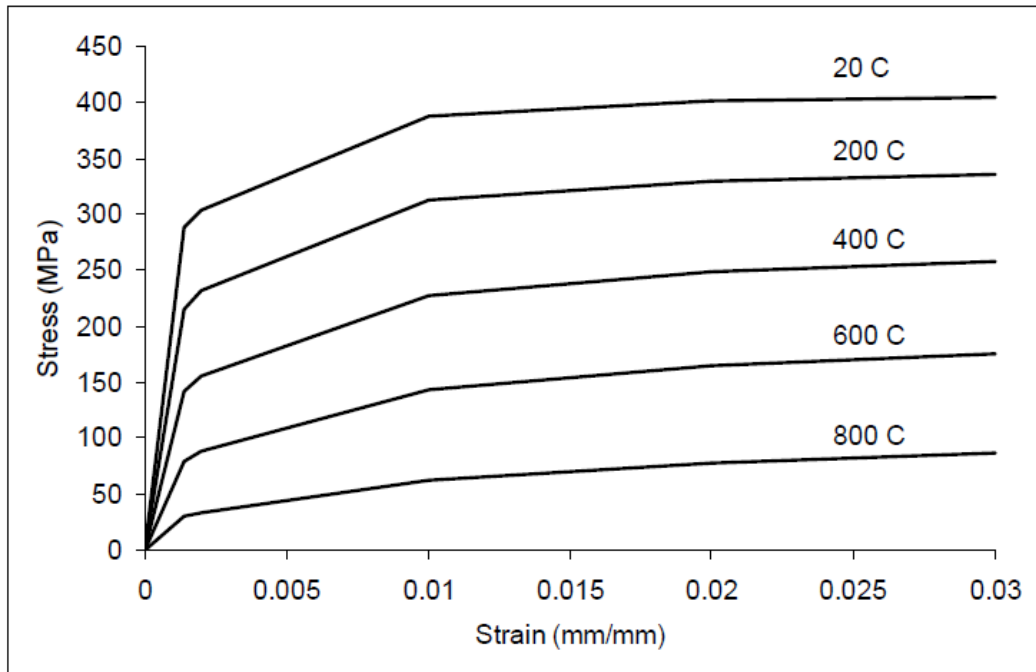
Eurocode 4 (Eurocode, 2005) proposes stress-strain curves for steel and concrete at elevated temperatures. Eurocode assumes steel behavior to be symmetric in tension and compression (i.e.

ignores local buckling in compression and strain hardening in tension), assumes zero strength of concrete in tension and neglects the effect of concrete confinement (i.e. assumes conservative post-peak behavior). Detailed equations and discussion on the curves can be found in Section 3 of Eurocode 4 (Eurocode, 2005). Figure 2.3 and Figure 2.4 shows the stress-strain plots for steel and concrete at elevated temperatures.

The material models for steel covered in literature are symmetric in tension and compression, not accounting for local buckling of outer steel plates and the associated strength reduction. Effects of local buckling of steel plates become more predominant for slender sections; hence a material model accounting for the same was considered. Lai et al. (2016) developed an effective stress-strain model for steel that considered strength degradation in compression and strain hardening in tension. This model was developed for steel at ambient temperatures and validated using experimental data. Further details of its development and validation are reported in Lai et al. (2016). This material model was modified to account for temperature effects, which is explained in the next chapter, and was compared with other existing steel material models.



(a)



(b)

Figure 2.1: (a): Concrete stress-strain curves at elevated temperatures developed by Lie (1992). Ref: Hong (2007); (b): Steel stress-strain curves at elevated temperatures developed by Lie and Irwin (1995). Ref: Hong (2007)

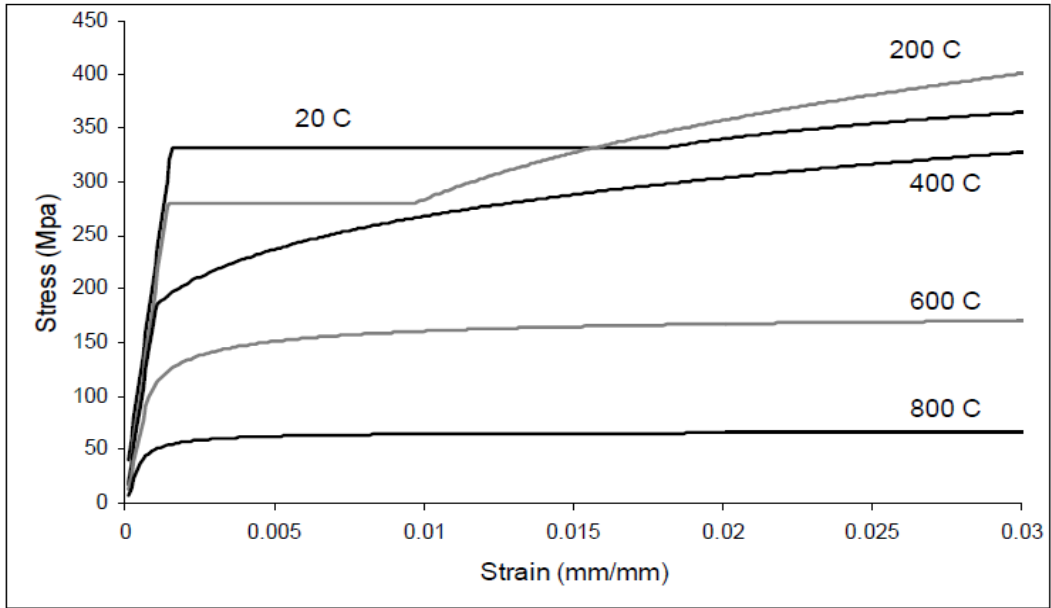


Figure 2.2: Stress-strain curves for 330 MPa steel developed using Poh's model. Ref: Hong (2007)

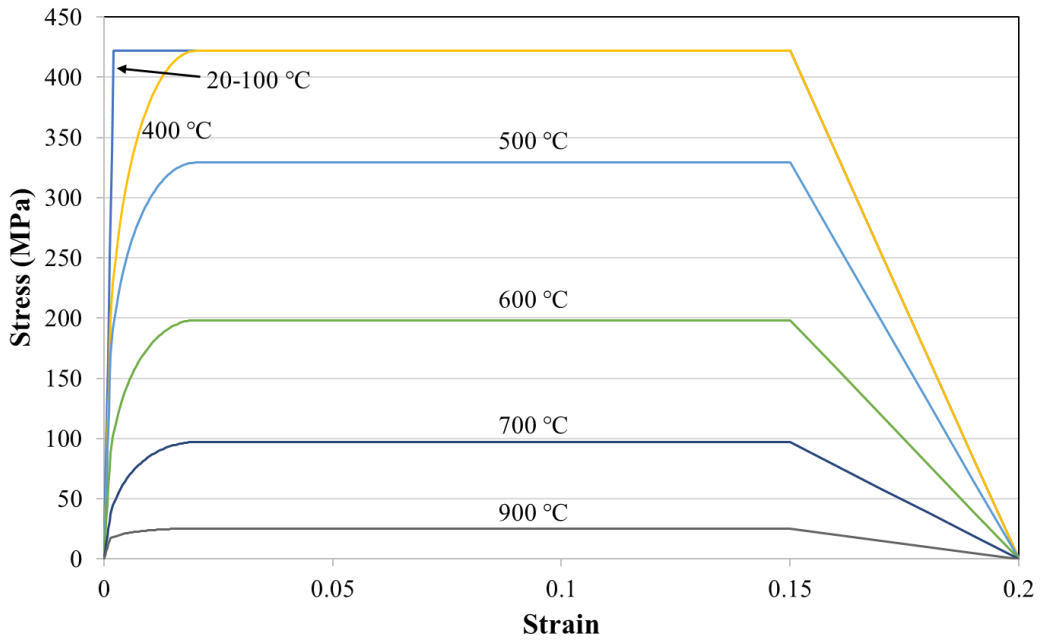


Figure 2.3: Eurocode stress-strain-temperature curves for 420 MPa steel

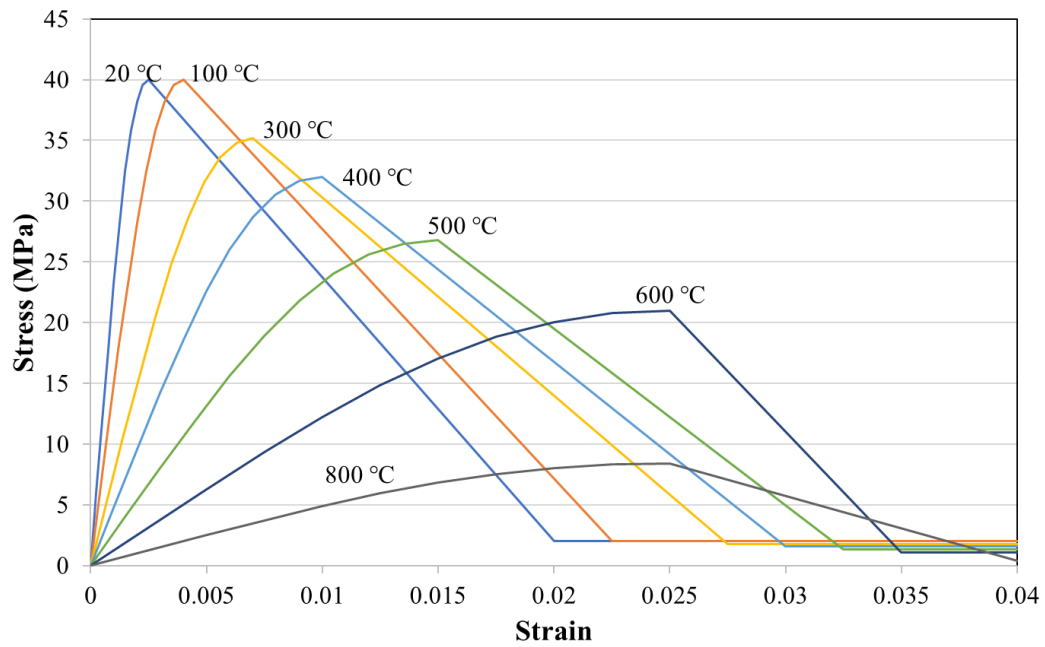


Figure 2.4: Eurocode stress-strain-temperature curves for 40 MPa concrete

### **3. 2D NUMERICAL MODEL- DEVELOPMENT AND BENCHMARKING**

A 2D fiber-based numerical model to simulate composite axial members under fire loading was developed in the current study. The goal was to develop a quick and accurate tool that could be used for analysis and design of composite members under fire loading. MATLAB (2006), a general-purpose computing software was used as a platform to develop this fiber model. A user-interface was also developed to allow easy interaction with the model and to conveniently view the results. This chapter presents the development, validation and benchmarking of the fiber model.

#### **3.1. Model Algorithm and Working**

The basic functionality of this fiber model was taken from the fiber model developed by Hong (Hong, 2007; Hong et al., 2009). However, the model was designed to be applicable to a wide range of applications, which include CFTs, composite walls (C-PSWs) and various fire scenarios. Validation of the model was done using experimental and 3D finite-element data.

The 2D fiber-model is a fundamental section-based model which involves modeling a cross-section of the axial member, typically at its mid-span. For the purpose of analysis, the cross-section is divided into discrete fibers consisting of nodes and elements. A representation on of the section discretized into fibers is shown in Figure 3.1. An incremental analysis is utilized, wherein the column is analyzed in its present state at each time step, and the analysis results used to update the column state for the next time step. At each time step, the procedure can be divided into 3 analysis steps, which are:

- 2D Heat Transfer Analysis
- Section Moment-Curvature Analysis
- Non-linear Column Buckling Analysis

The details of each step, its assumption and simplifications are outlined as follows:

##### *3.1.1. 2D Heat Transfer Analysis*

In the first step (2D heat transfer analysis) the temperature of each node and element of the section is calculated based on applied thermal material properties. Heat transfer always occurs

from the object at the higher temperature to the object at the lower temperature. Heat can be transferred in three different ways: conduction, convection, and radiation. Conduction is the transmission of heat between two solid objects that are in contact. Convection is the transmission of heat between a solid object and moving fluid that are in contact with each other. Radiation is the heat transfer between any two objects (solid, fluid, or gas) in the form of electromagnetic waves. These three modes of heat transfer are represented in Figure 3.2. The heat balance equations between objects can be setup by considering all the contributions of energy. These equations in their finite difference form can be solved numerically.

The first step of this heat transfer analysis is defining the surface temperatures, which are assumed constant along the length of the column. Multiple time-temperature curves are programmed into the model to specify the surface temperature, to provide flexibility of analysis. Also, the user can choose to directly specify the surface temperature or specify a gas temperature and calculate the surface temperature considering convection and radiation. The modeling of thermal conductivity, specific heat and other equations related to heat transfer are reported in Hong et al. (2009) and are not repeated here. A schematic flowchart of the algorithm is shown in Figure 3.3. A layer of fire protection can also be modeled outside the steel surface. If modeled, the thermal properties of fire protection are assumed to remain constant with temperature.

There are two heat-transfer algorithms, one of which is called depending on the model being run. The symmetric heat-transfer algorithm considers all four sides of the column to be heated, thus heat transfer within the section is doubly symmetric and there is no heat loss from the member to the air. The non-symmetric heat-transfer algorithm is called for one or three-sided heating. In this case, heat is absorbed by the column from the heated surfaces and the unheated surfaces lose heat to the atmosphere. The extent of heat loss can be controlled by adjusting the convection coefficient, which is a user-defined parameter. The element temperatures thus obtained are used to determine material properties as outlined in the next steps.

### *3.1.2. Section Moment-Curvature Analysis*

The next step of the analysis involves generating a cross-section moment-curvature plot for the applied axial load and the calculated temperatures in the heat transfer analysis. In this step, the curvature is started from  $0 \text{ m}^{-1}$  and increased in increments  $0.001 \text{ m}^{-1}$  to  $0.35 \text{ m}^{-1}$ . The section moment for each curvature value is calculated using an iterative process. An initial centroidal strain

is assumed and its value adjusted based on section equilibrium (i.e. summation of element forces equals the applied axial load). Element total strains are calculated from curvature and centroidal strain based on the plane sections assumption. Thermal strain is also calculated for each fiber from its coefficient of thermal expansion and temperature change. The mechanical strains are then obtained by subtracting thermal strain from total strain. Mechanical strain of each element is provided as input to the material stress-strain-temperature ( $\sigma$ - $\epsilon$ - $T$ ) models to get stresses in the elements. Once force equilibrium is established, net moment of the section is calculated by summing up the moment contribution of each element. The obtained moment-curvature plot is then used in column buckling analysis.

Multiple stress-strain-temperature material models are programmed in the model to allow flexibility of analysis and the comparison of different proposed models. In all these models, concrete strength in tension is assumed zero and strain hardening of steel in tension is ignored. Different material models and their combinations are discussed further in this chapter. Further detailed steps and equations to obtain strains and stresses and moment are detailed in Hong (2007) and Hong et al. (2009). A pictorial flowchart of the algorithm is shown in Figure 3.4.

### 3.1.3. *Non-linear Column Buckling Analysis*

The last step (non-linear column buckling analysis) utilizes a modified version of Newmark's method of inelastic column buckling analysis to simulate the overall column behavior. Newmark's method is modified to be applicable for elevated temperatures, by using the moment-curvature plots generated in step 2. The column is discretized into several stations along the length and a slice or station point is assumed to be located at the center of each segment. Further, a fiber model of the CFT cross section is assumed to be located at each slice or station point.

After obtaining the temperature distribution and moment-curvature curve (which hold for every station point), the section primary and secondary moments are obtained due to load eccentricity and lateral displacement. The lateral displacements ( $v_{i,j}$ -assumed) at each station (j) are assumed based on the displacements in the previous time step ( $t_{i-1}$ ). For the first time step, lateral displacements at each station are assumed based on the geometric imperfection. Load eccentricity is measured from the center of stiffness of the section, which may change with time for non-symmetric heating.

The calculated station moments are used to calculate station curvatures using the moment-curvature plot obtained in Step 2. An updated deflected shape (lateral displacement) is found by twice numerically integrating the curvature values. This updated shape is compared to the assumed shape at the beginning of the time step and iterations are carried out till convergence. Detailed procedure and equations for this step are reported in Hong (2007) Hong et al. (2009).

The model checks for two modes of failure of the column, which are global buckling (instability) and yielding/crushing. The column is considered to have failed due to global instability when the maximum moment along the column length (typically at mid-span) exceeds the maximum moment that can be developed in the section (maximum moment in  $M-\phi$  curve). The column is considered to fail in yielding if axial force equilibrium cannot be established at any step while generating the moment-curvature plot. This failure mode governs for short columns whereas longer columns typically undergo global instability failure. A pictorial flowchart of the algorithm is given in Figure 3.5.

### **3.2. Material Stress-strain-temperature Models**

Material stress-strain-temperature models form a crucial part of the 2D fiber-based analysis tool. They have a significant effect on the behavior of the member, as discussed further in this thesis. Additionally, material behavior at elevated temperatures is complicated as discussed previously and thus the material models are at best an approximation of true material behavior. Some of the relevant material models developed by researchers (discussed in the previous chapter) have been programmed into the fiber model.

Multiple material models were programmed in the fiber model which allows the user to select the desired material model. Most of the models are taken directly from literature [2.3]. However, the effective stress-strain model for steel, developed by Lai et al. (2016) was modified in this study to work for elevated temperatures. This modification and different material model combinations available to the user are covered here.

Lai et al. (2016) developed effective stress-strain curves for steel for non-compact and slender CFTs which accounted for local buckling of steel faceplates in compression and strain hardening in tension. The detailed development and validation of these equations is covered in Lai

et al. (2016). Figure 3.6(a) shows the steel stress-strain curves for compact, non-compact and slender sections at ambient temperature.

The equations developed by Lai et al. (2016) were modified in this study to work for elevated temperatures. These modifications involved updating the stiffness, yield strength and post-buckling strength in compression as a function of temperature. The equations for temperature dependence of yield strength ( $\sigma_y$ ) and Young's modulus ( $E_s$ ) were taken from the steel material model developed by Poh (2001). The stress-strain-temperature curves obtained using these equations are given in Figure 3.6(b).

The relative behavior of different combinations of material models was explored and is covered in the sub-section discussing the benchmarking of the fiber model.

### **3.3. Fiber-Model Validation and Benchmarking**

Validation of the fiber model developed by Hong et al. (2009) involved comparison with experimental data obtained by various researchers and finite-element models developed by Hong et al. (2008). Detailed validation of the model is covered in Hong (2007) and Hong et al. (2009) and a representative comparison graph generated by Hong et al. (2009) is given in Figure 3.7. The figure shows the temperature versus time and axial displacement versus time for a square CFT specimen, with plots obtained from experiment, 3D FE model and the fiber model plotted together. It is evident that the fiber model is reasonably accurate in predicting the failure time and axial displacement. Similar plots were generated for various other specimens tested by Hong.

For the fiber model developed in this study, validation was carried out using experimental data and FE analysis results. Model validation mainly focused on rectangular CFTs and walls, as square CFTs had been extensively studied by Hong. Validation and benchmarking were done for two scenarios: ambient temperatures and elevated temperatures.

#### *3.3.1. Ambient Temperatures*

Validation and benchmarking at ambient temperatures aimed at validating Newmark's nonlinear buckling algorithm. It was done by comparing fiber model results with experimental tests conducted on CFTs at ambient temperatures and design equations given in Chapter I of AISC 360 (AISC, 2016).

The results obtained from the fiber-model were compared with the capacity equations given in AISC 360 Specification (Chapter-I, Eqn. I2-2 to I2-13). Figure 3.8 shows the normalized load versus axial displacement plots for compact, non-compact and slender CFT sections for conventional and effective steel models. Results obtained using conventional (elastic-perfectly-plastic) and effective (Lai et al. 2016) steel models are shown in Figure 3.8(a) and Figure 3.8(b) respectively. The load is normalized against the predicted column capacity per AISC 360 (Chapter I). Fiber model predicted buckling of columns close to the AISC predicted critical load. Hence the capacity predicted by the fiber model (at ambient temperature) has good agreement with the capacity estimated per AISC 360.

Further, the fiber model was validated against data from the experiments conducted by Lue et al. (2006). They tested a total of 30 rectangular CFT column specimens at ambient temperature with varying concrete strength. Details of all the specimens tested and the obtained results are reported in Lue et al. (2006). The comparisons of experimental, fiber-model predicted and AISC 360-16 (Chapter I) predicted strengths for the specimens is given in Table 3.1. It is evident that the fiber-model predicts strengths that are in between experimental and AISC predicted values, confirming its accuracy.

Comparisons with AISC 360 predicted capacity were used for benchmarking of the fiber model for the appropriate material model for steel. On comparing Figure 3.8(a) and (b) it is evident that effective stress-strain curves are more accurate for non-compact and slender sections (as the failure is closer to 1). For compact sections, effective stress-strain model was seen to be over-conservative. This is because local buckling of steel faceplates is significant only for non-compact/slender sections. Conventional (elastic-perfectly-plastic) stress-strain model gives better results for compact sections, as it does not consider local buckling. Eurocode models also do not consider local buckling and hence should be used only for compact sections.

### *3.3.2. Elevated Temperatures*

At elevated temperature, model validation was aimed at verifying the heat transfer algorithms and material stress-strain-temperature models. The temperature profiles across the section of C-PSW specimens were compared with experimental data and 3D FE results (Taghipour Anvari et al., 2020b). This comparison was done for both symmetric and non-symmetric heating. The steel surface temperature at failure of different wall specimens as predicted by the fiber model

and by 3D FE analysis was also compared (Bhardwaj et al. 2019b). Figure 3.9(a) shows the comparison of temperature profile through the thickness of a 200 mm thick wall at two time instants obtained from FE analysis and the fiber model. Figure 3.9(b) shows the comparison of temperature variation with time for non-symmetric heating as obtained from experimental data and as predicted by the fiber model. Table 3.2 presents the failure surface temperature predicted by FEM and the fiber model for 6 wall specimens (Table 5.1). This data is graphically plotted in Figure 3.10.

It is evident from Figure 3.9(a) and (b) that the temperature profiles from the fiber model show a close match to FEM results and experimental data, both for symmetric and non-symmetric heating. The slight discrepancies are expected considering the simplifying assumptions of the fiber-model. The steel surface temperature at failure for C-PSWs/CF also are reasonably similar to FEM results (Table 3.2, Figure 3.10). It can thus be stated that the fiber model provides good accuracy while modeling CFTs and walls. Further comparisons of wall behavior as predicted by fiber model and finite-element models is done in 5.

For benchmarking of the fiber model at elevated temperatures, results for C-PSWs and CFTs were compared with FE analysis and experimental data. Six different combinations of material models of steel and concrete were tested for C-PSWs and CFTs. Comparisons were done by studying the axial displacement versus time plots and axial displacement versus temperature plots. The combinations of material models tested are stated in Table 3.3 and the obtained comparisons are presented and discussed here.

The wall specimen for which different material models were tested was CW-200-20-20 (Table 5.1). The obtained plots are shown in Figure 3.11. Peak axial displacement is seen to be dependent only on the steel material model. As concrete strength in tension is ignored in all material models, it does not influence wall behavior for positive axial displacements. Whereas the concrete model has a significant effect on the post-peak behavior of the wall, with a clear increase in time to failure for Lie's confined concrete model. However, the confined concrete model overestimates the wall capacity compared to FE results. Thus, the effect of confinement of concrete is not very prominent in C-PSWs. It is recommended to use Eurocode defined material model for concrete for walls.

Further, a CFT column having overall dimensions 300 mm x 300 mm with steel faceplate thickness 9 mm and height equal to 3.5m was modeled. Axial load equal to 2020 kN was applied. The obtained axial displacement against time and temperature plots for the six material model combinations are shown in Figure 3.12. Similar behavior was observed for the CFT column, with steel material model governing the peak axial displacements and the steel and concrete models influencing the time to failure. However, concrete material model has a lesser impact on CFT post-peak behavior as compared to walls. The difference in time to failure for Eurocode's concrete model and Lie's concrete model is not as significant, as observed for C-PSWs. Comparing these results with experimental data for the same specimen (Hong, 2007) it is observed that Poh's steel model gives axial displacements which are closest to the experimental data. Although concrete model does not have a high impact on CFT behavior, the Eurocode concrete model shows better agreement with experimentally observed failure times.

### **3.4. Limitations of the fiber model**

The 2D fiber model provides a quick and accurate tool for analysis and design of composite axial members. However, the tool faces certain limitations as a result of the simplifying assumptions made. These major limitations and assumptions are discussed as follows:

- The fiber model provides only 2 degrees of freedom for strains, i.e. centroidal longitudinal strain and curvature, making it more restricted than 3D models.
- The fiber model assumes plane sections remain plane and perpendicular to the neutral axis at every discrete location (station) along the length. Between two discrete points, the section curvature is assumed to be interpolated, which is a major limitation.
- The fiber model uses uniaxial stress-strain-temperature models for steel and concrete. The multiaxial stresses and strains are not accounted, and are assumed to have no influence on the longitudinal (uniaxial) stress-strain-temperature behavior.
- As a result of the previous assumption, the effect of concrete infill applying a lateral pressure on steel faceplates (thus increasing their tendency to buckle outwards) is not accounted for.

- In the case of C-PSWs, the effect of ties and shear studs causing local variations in heat transfer is ignored and they are not modeled. Tie bar spacing is considered only to determine section slenderness

### **3.5. Development and Functioning of User Interface**

A Graphical User Interface (GUI) was developed for the tool with the aim of enhancing its usability and giving designers the ability to better manipulate the inputs and visualize the results. The GUI was developed using MATLAB App Designer, R2018b. The interface was designed with the ability to run the model in multiple ways depending on the user and display the results as interactive plots. The structure of the interface can be divided into two main components, namely, a pre-processor and a post-processor. This structure and displays are explained in the following sub-sections.

#### *3.5.1. Pre-Processor*

The pre-processor is the first step of the UI implementation. It takes the inputs from the user, which include geometric and material properties of the column/wall, loading conditions and fiber discretization. Most of the inputs have in-built default values, which are fed to the tool if the user does not provide anything. The pre-processor also determines how to run the fiber model, based on the inputs of the user. The UI provides the option of using the model as a simple analysis tool, using the model for parametric studies, or using it as a design tool. A section for advanced options is also provided if the user wants to change the finer details of the model. The pre-processor interface and advanced options tab are shown in Figure 3.13(a & b).

#### *3.5.2. Post-Processor*

The post processor provides the user with various options to view the results. This part of the UI is called after the simulations have been run, and it takes the output variables from the main code. The post-processor then generates interactive visual outputs of Temperature, Axial and Lateral Deformations, Stress, Strain and Moment-Curvature. For each plot, the user has multiple options of viewing the results, and while running the program in design mode, the post-processor allows the user to visualize the allowable design values. A few examples of the post-processor outputs are shown in Figure 3.14.

Table 3.1: Comparison of experimental, fiber-model predicted and AISC 2016 predicted compressive strengths at ambient temperature

<b>Specimen No.</b>	<b>Notation</b>	<b>Average Experimental Strength (kN)</b>	<b>Fiber model Predicted Compressive Strength (kN)</b>	<b>Compressive Strength from AISC Manual 2016- Nominal (kN)</b>
1	C0K 2-1-2	1059.7	NA	715.0
2	C4K 4-1-4	1328.5	1075	1004.1
3	C9K 6-1-6	1722.3	1425	1323.8
4	C10K 6-1-6	1885.5	1500	1388.3
5	C12K 6-1-6	2089.8	1625	1516.2

Table 3.2: Comparison of failure surface temperature for 6 wall specimens from FE analysis and fiber-model

<b>Nomenclature</b>	<b>Height (mm)</b>	<b>Slenderness (H/d)</b>	<b>FEM predicted failure surface temperature (°C)</b>	<b>Fiber model predicted failure surface temperature (°C)</b>
CW-300-10-20	3000	10	1084.88	1171.8
CW-300-15-20	4500	15	1047.95	1100.1
CW-300-20-20	6000	20	1041.03	1033.7
CW-200-10-20	2000	10	1058.2	1073.5
CW-200-15-20	3000	15	1025.15	999.82
CW-200-20-20	4000	20	968.273	938.2

Table 3.3: Various combinations of material models tested

<b>Model ID</b>	<b>Steel model</b>	<b>Concrete Model</b>
Model 1	Eurocode	Eurocode
Model 2	Eurocode	Lie Confined
Model 3	Effective $\sigma$ - $\epsilon$	Lie Confined
Model 4	Poh	Lie Confined
Model 5	Poh	Eurocode
Model 6	Effective $\sigma$ - $\epsilon$	Eurocode

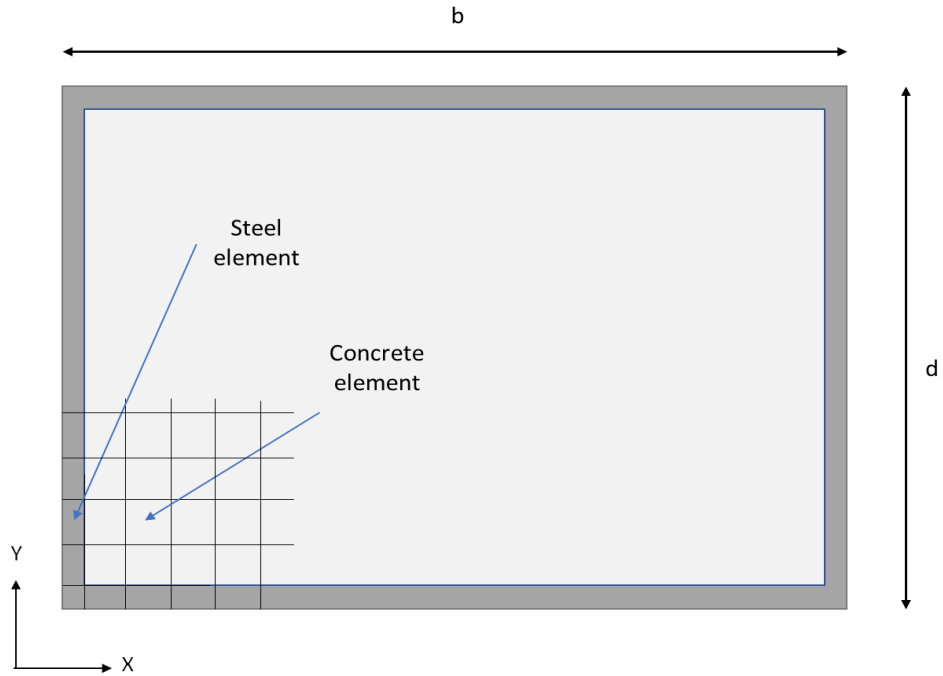


Figure 3.1: Representation of CFT section discretized into fibres

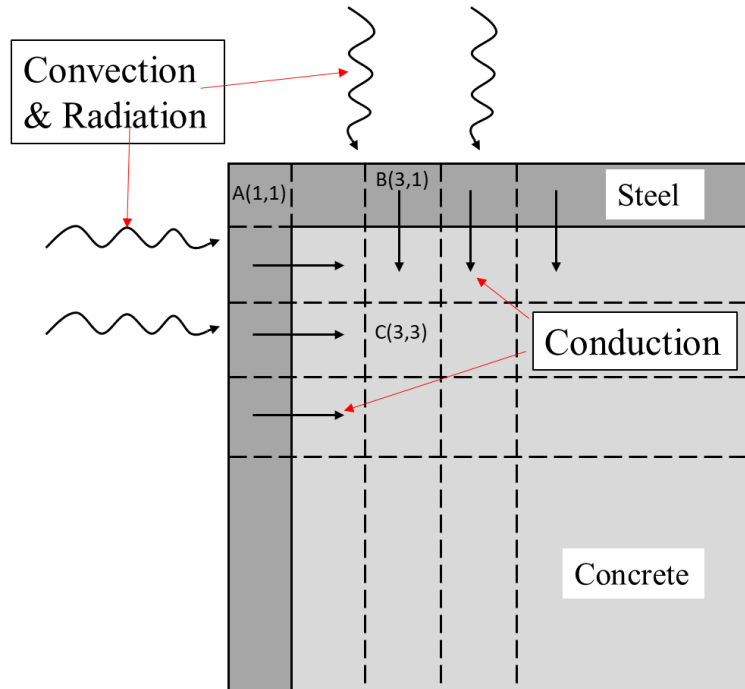


Figure 3.2: Representation of the three modes of heat transfer: convection, conduction & radiation

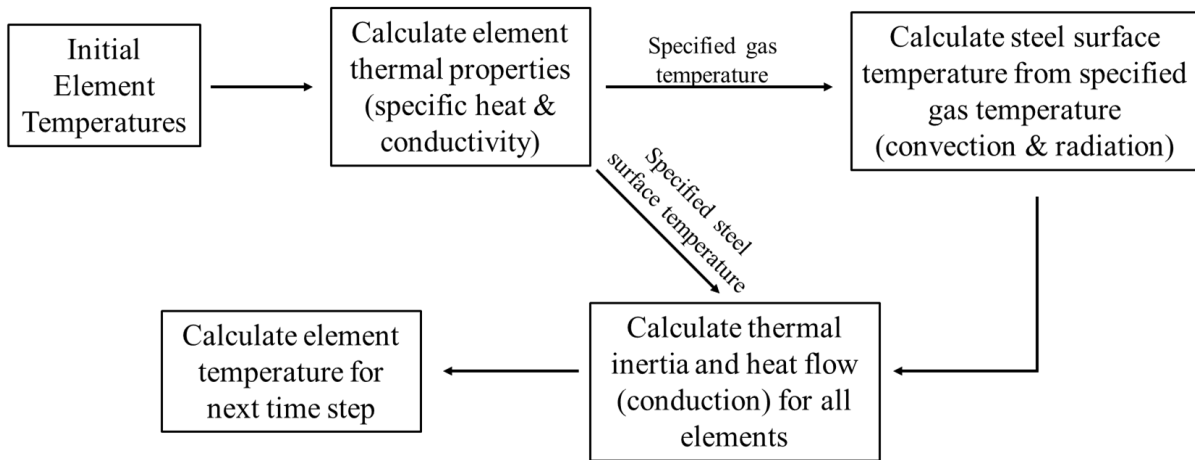


Figure 3.3: Schematic flowchart of algorithm for 2D heat transfer

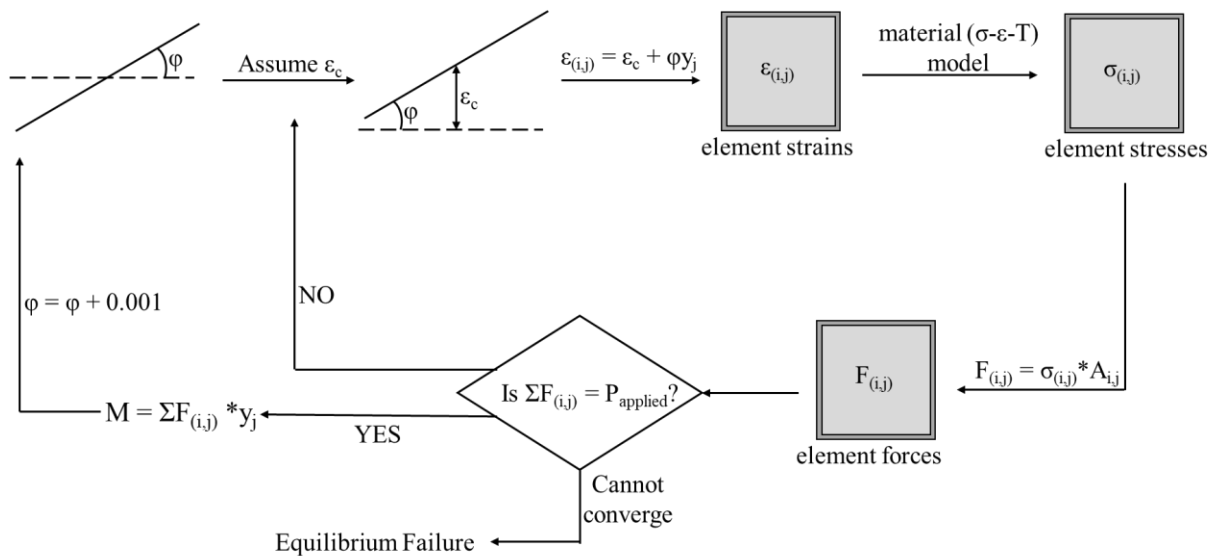


Figure 3.4: Flowchart showing the algorithm to generate Moment-Curvature Plot

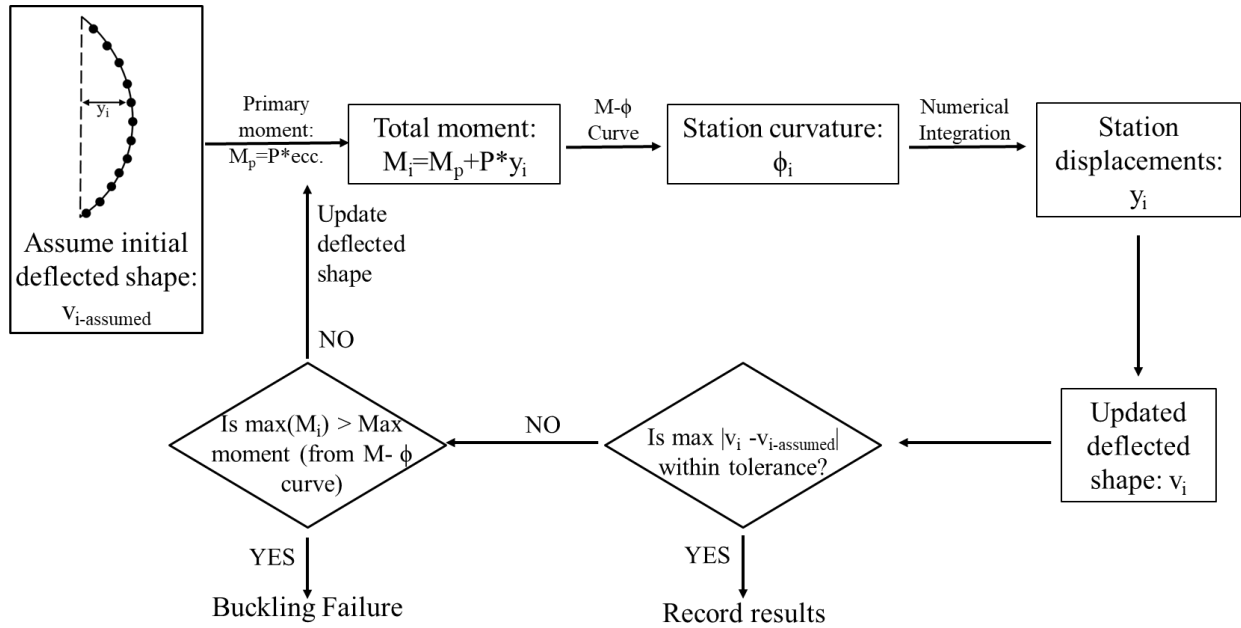
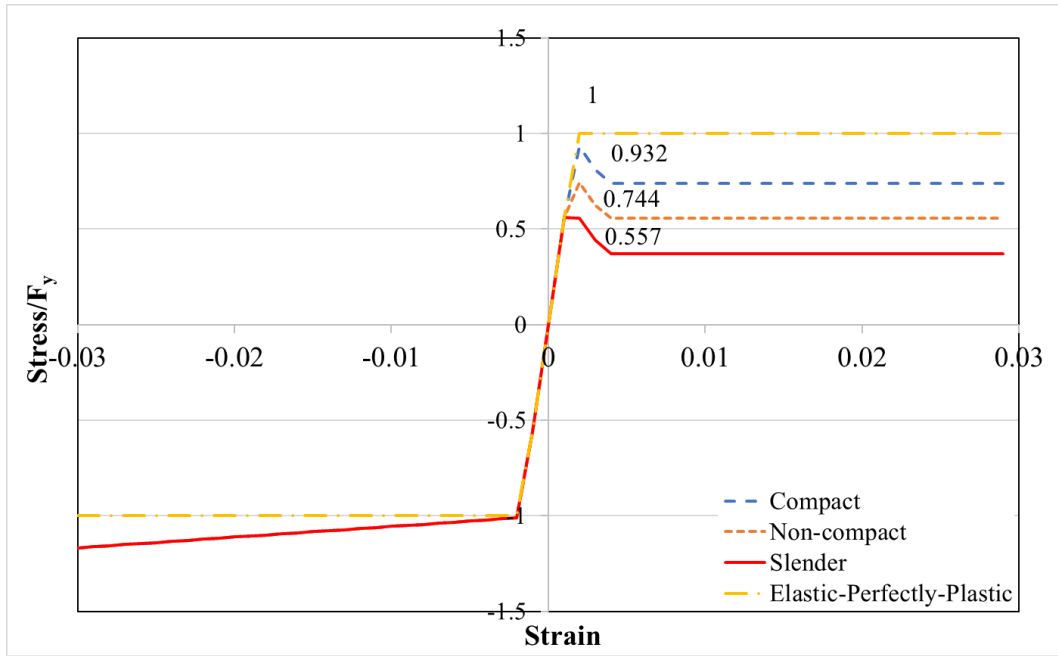
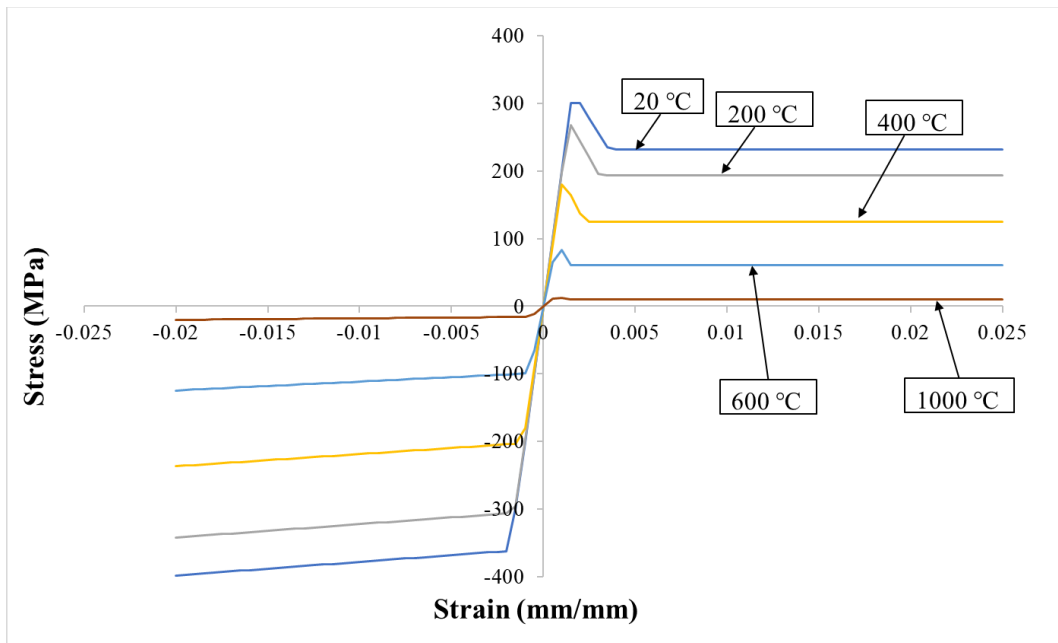


Figure 3.5: Flowchart showing the algorithm of Newmark's Inelastic Column Buckling Analysis



(a)



(b)

Figure 3.6: (a) Effective stress-strain curves for compact ( $\lambda=50$ ), non-compact ( $\lambda=67$ ) and slender ( $\lambda=100$ ) sections for steel ( $F_y=358$  MPa) at ambient temperature; (b) Effective stress-strain curves for 330 MPa steel at elevated temperatures

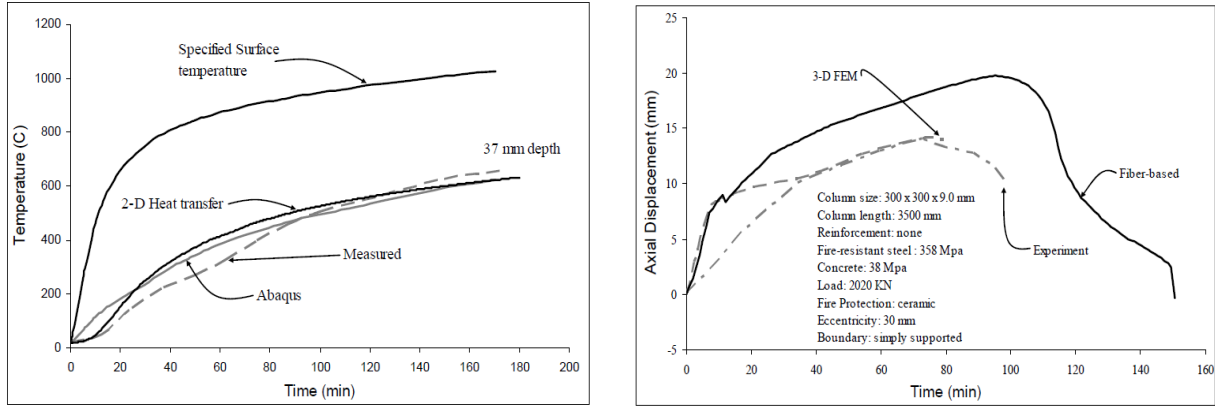


Figure 3.7: Representative validation of the Fiber Model carried out by Hong. Ref: Hong (2007)

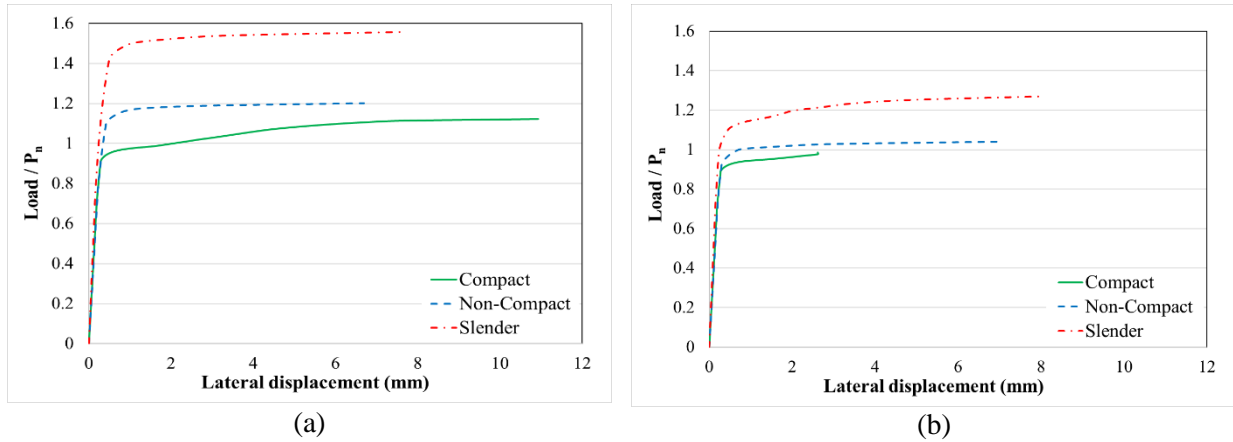
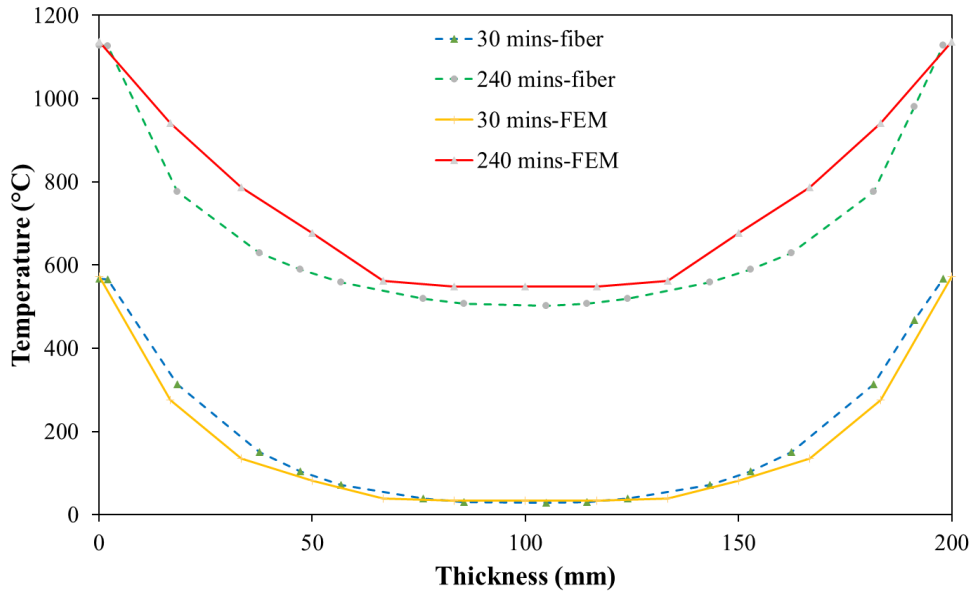
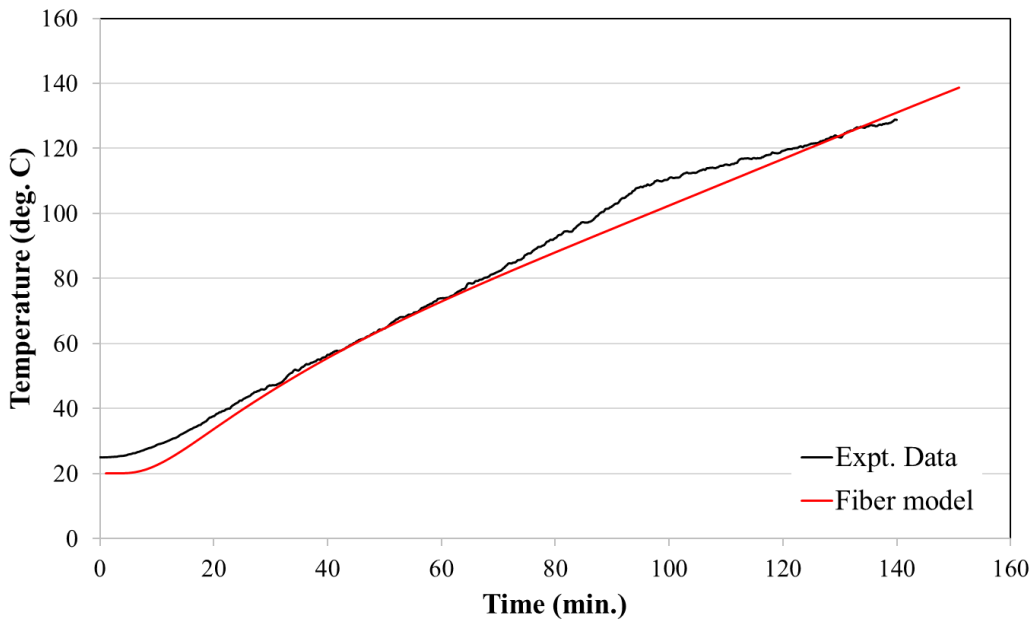


Figure 3.8: Comparison of compressive strength (load vs. lateral displacement) for (a) conventional (elastic-perfectly-plastic) and (b) effective (Lai et al. 2016) steel models versus AISC (2016) predicted strength



(a)



(b)

Figure 3.9: (a) Temperature profiles across the section at various time instants; Comparison of fiber model predicted and FEM data; (b) Surface temperature vs time for 3-sided heating: comparison of experimental data and fiber model. The plot shows the temperature of a point on the un-heated surface

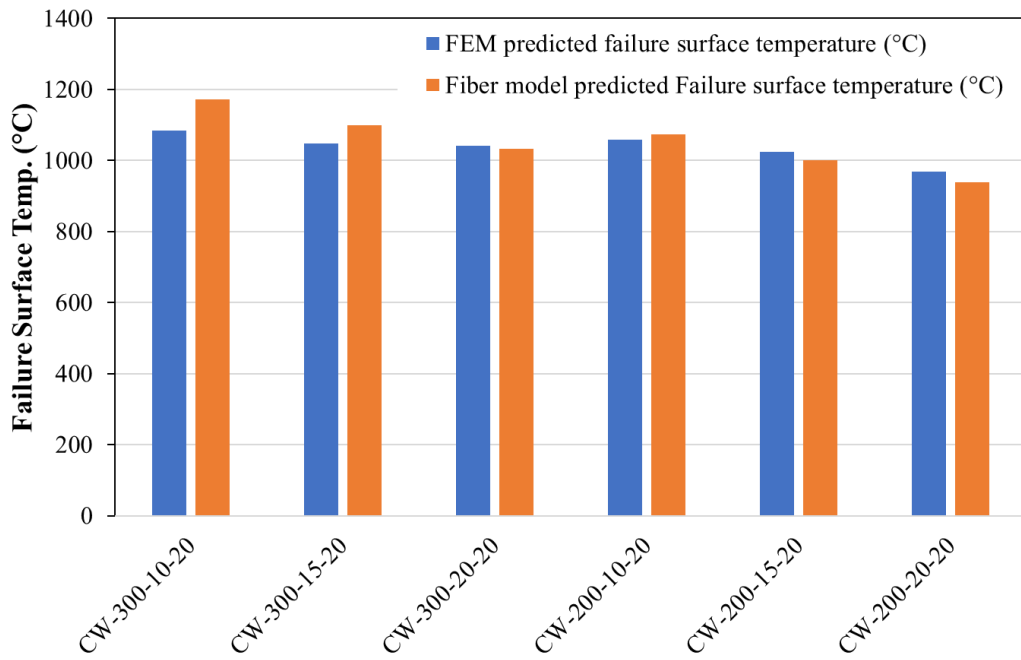
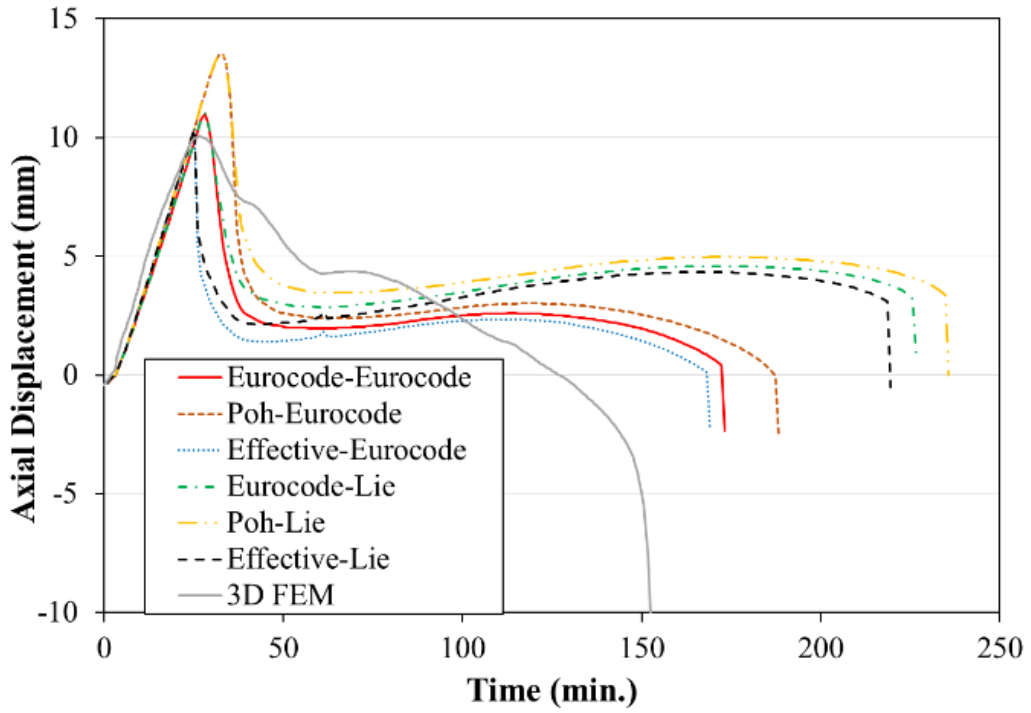
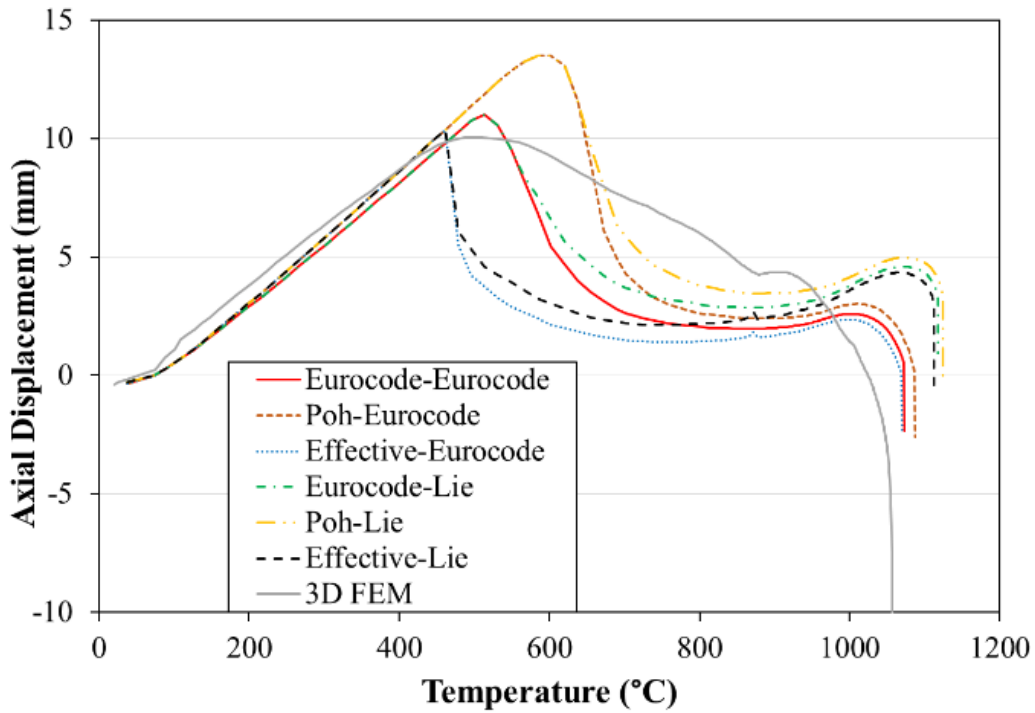


Figure 3.10: Comparison of steel surface temperature at failure as predicted by the fiber-model and FE analysis for C-PSWs

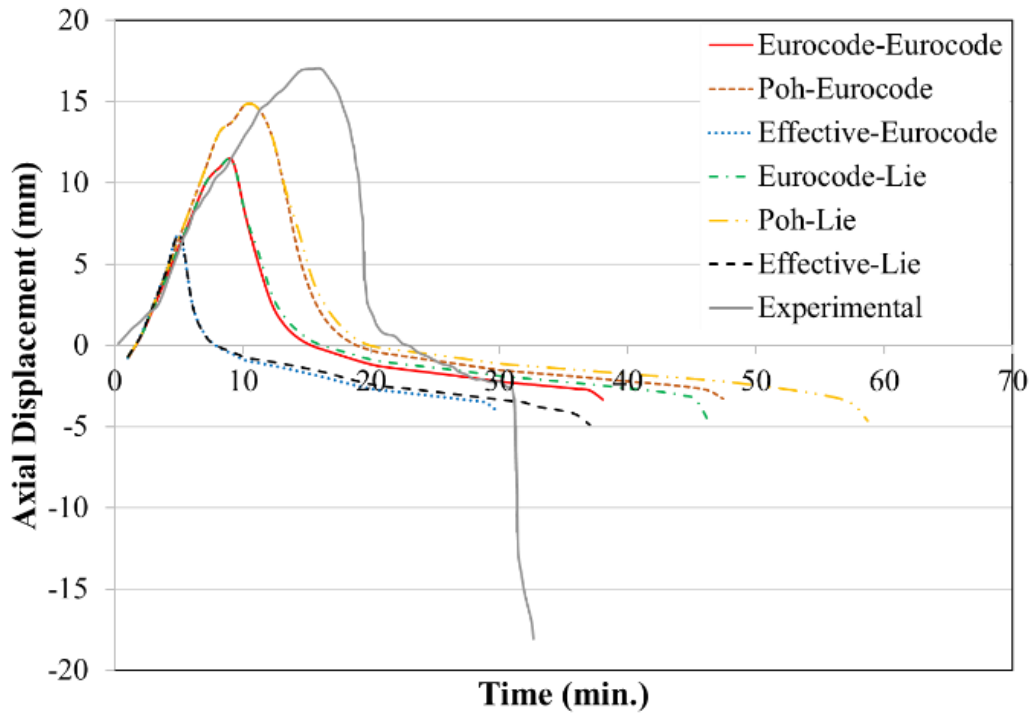


(a)

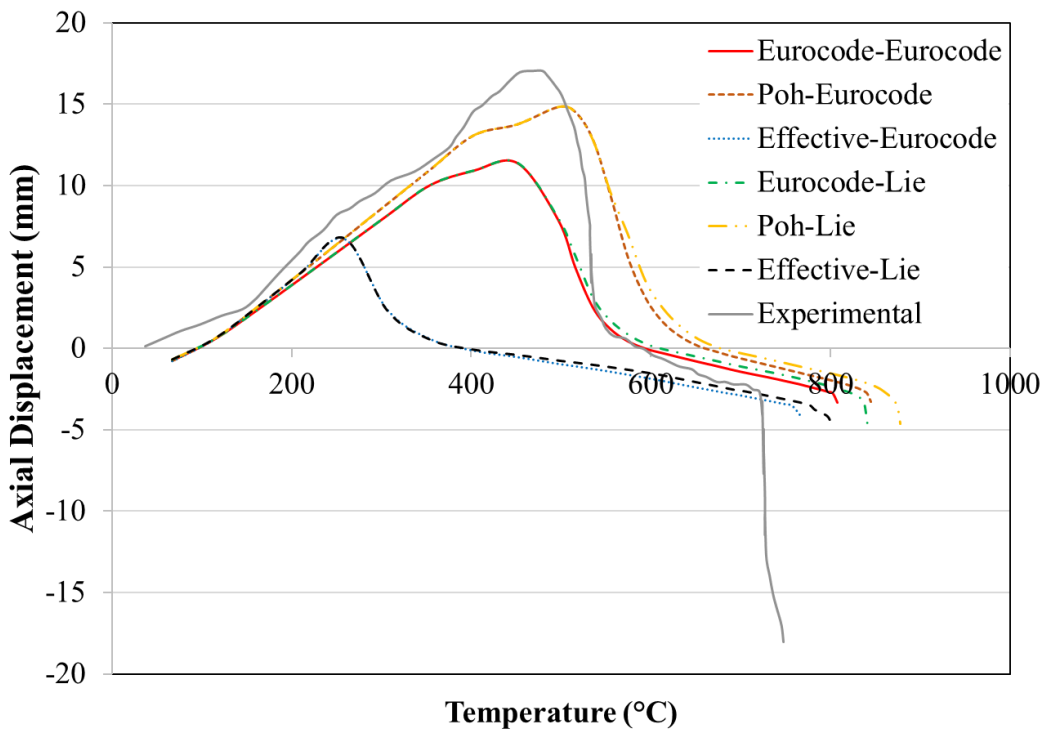


(b)

Figure 3.11: (a) Axial displacement vs time and (b) Axial displacement vs temperature for the wall specimen for different combinations of material models, plotted with the FE analysis obtained curve; The curves are labelled by the steel and concrete model respectively



(a)



(b)

Figure 3.12: (a) Axial displacement vs time and (b) Axial displacement vs temperature for the CFT specimen for different combinations of material models, plotted with the FE analysis obtained curve; The curves are labelled by the steel and concrete model respectively

#### Geometric Properties

Width of Column (m)

Depth of Column (m)

Thickness of Steel Face Plate (m)

Length (m)

Length/Imperfection

#### Material Properties

Compressive Strength of Concrete (MPa)

Yield Stress of Steel (MPa)

Limiting Strain of Concrete

Limiting Strain of Steel

Density of Steel (kg/m3)

Density of Concrete (kg/m3)

#### Loading

Pn - Nominal Compressive Strength (KN)

Initial Load/Pn

Initial Surface Temperature (°C)

Eccentricity of Load (m)

**Find Nominal Compressive Strength**

#### Fiber Discretization

Number of Stations in the beam-column

Number of Concrete Elements along x

Number of Concrete Elements along y

**How does the Fiber Model work?**

**Advanced Options**

Fire Analysis  
 Ambient Analysis

#### Time

Maximum time (in minutes)

Desired Time Step (in minutes)

**Submit Inputs**      Total Time Computed:  minutes

#### Key Outputs (at failure):

Time to failure (in minutes):

Surface Temperature of Steel (°C):

Axial Deformation (mm):

Maximum Lateral Deformation (mm):

Average Temperature of Concrete (°C):

#### Detailed Outputs/Plots

**Design:**

(a)

### Advanced Options:

Rebar Section in Lie's Column Test

Stress-Strain Curve

Surface Temperature Case

#### Fire Protection Layer Properties

Thickness of Fire Protection Layer (m)

Density of Fire Protection Layer (kg/m3)

Convection Coefficient (W/(m<sup>2</sup>·K)):

Stefan-Boltzmann Constant: (W·m<sup>-2</sup>·K<sup>-4</sup>)

Emissivity of Fire Protection Layer

Emissivity of Fire Smoke

Thermal Conductivity of Fire Protection Layer: (W/(m·K)):

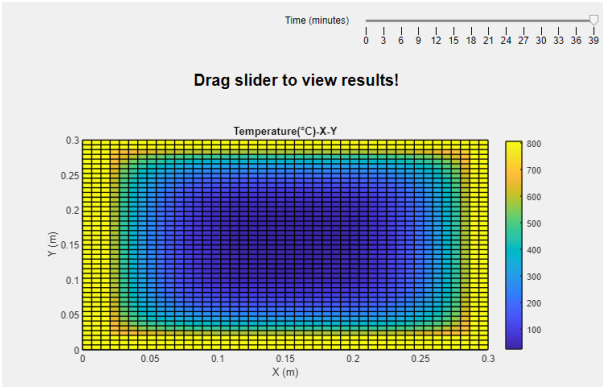
Specific Heat of Fire Protection Layer: (J/(K kg))

**If 4/7 is selected in Stress-Strain Curve, program takes 4 for compact and 7 for non-compact and slender sections.**

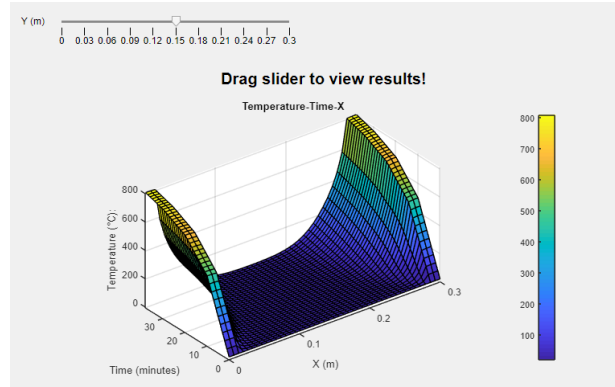
**Submit**

(b)

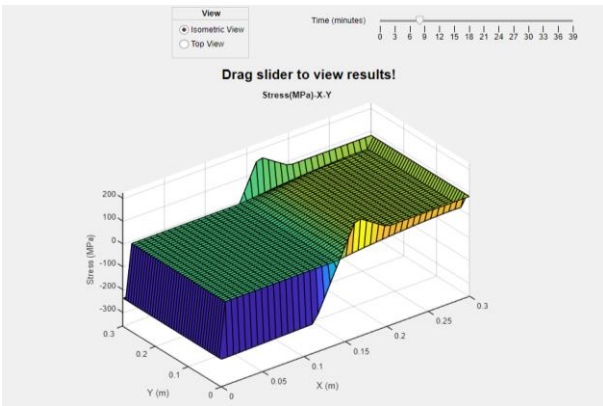
Figure 3.13: (a) Pre-processor interface of the UI, with all input variables (b) Advanced options interface of the UI



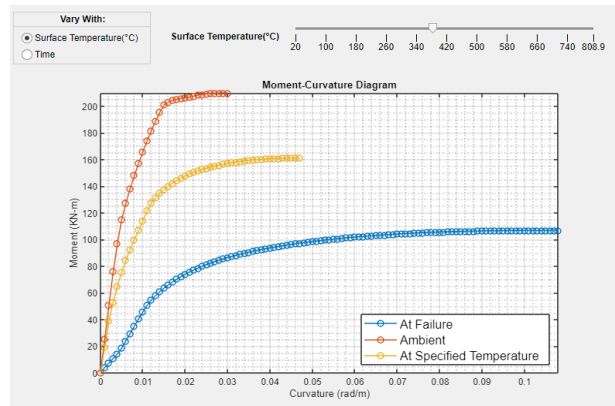
(a)



(b)



(c)



(d)

Figure 3.14: Examples of post-processor output interfaces

## **4. CFT PARAMETRIC STUDY AND CAPACITY PREDICTION**

The second part of the study involved analyzing CFT and C-PSW specimens under fire loading using the fiber-model discussed in the previous chapter. Detailed discussion on the analysis of CFT columns is covered in this chapter while C-PSWs are covered in the next chapter.

For CFT columns, the analysis involved studying different aspects of CFT column behavior and the parameters affecting them. Geometric and material parameters were studied in a parametric study on CFT columns. The goal of these studies was to understand how these parameters influence CFT behavior. In the parametric study, a constant axial load was applied while the column surface was subjected to uniform elevated temperatures following the ASTM E119 standard time-temperature curve. The effect of a layer of fire protection on the steel surface was also analyzed. The variation of effective stiffness of a CFT with time and relative contribution of concrete to this stiffness was also studied. Finally, an equation for capacity prediction of CFTs was proposed based on these results.

### **4.1. Parametric Studies**

The first part of the study on CFTs involved analyzing the effects of geometric and material parameters. Four parameters were considered in the parametric study namely aspect ratio of the column section (ratio of width to depth), reinforcement ratio/section slenderness (steel faceplate thickness), steel yield strength and concrete compressive strength. For each case, simulations were run for column slenderness of 5, 10, 15, 20, 30 and 50 and the axial load was increased from 10% to 100% of ambient nominal capacity in increments of 10%. The nominal axial capacity of CFTs was calculated per AISC 360-16, Chapter I. Based on the parameters to be studied, a parametric study matrix was developed. This matrix is given in Table 4.1. The nomenclature of the models presents the properties of the models in the order of aspect ratio, section slenderness, steel yield strength and concrete compressive strength.

All cases were considered to be without fire protection as the effect of fire protection was separately studied. Plots form the four series and the results are further discussed in detail in the following sub-sections.

#### 4.1.1. Section Aspect Ratio

The column aspect ratio (ratio of column depth to width) was studied as a variable parameter. The cases were taken such that aspect ratio increased from 1 (C-1.0-50-358-38) to 2 (C-2.0-50-358-38) while section area and section slenderness remained nearly constant. The results are presented in a critical load against slenderness plot at two surface temperatures, which is shown in Figure 4.1. In the figure, the curves are plotted for surface temperatures of 400 °C and 900 °C and the curves are identified by their aspect ratio in the legend.

The aspect ratio does not have a very significant effect on column capacity at 400 °C and 900 °C (Figure 4.1). While the column capacity increased slightly going from a ratio of 1 to 1.5 (for both 400 °C and 900 °C), it dropped again when the aspect ratio was further increased to 2. This is because as the depth of the column decreases (increasing aspect ratio), both moment of inertia ( $I = bd^3/12$ ) and length ( $L = \text{slenderness} \times d$ ) reduce for a given column slenderness. As critical buckling load is a function of the ratio of effective stiffness to length, it is unaffected. However, increasing the aspect ratio further would bring down the capacity as the effect of concrete confinement would reduce. In this study, the aspect ratio was limited to 2 as columns in practice rarely have higher aspect ratios.

#### 4.1.2. Cross Section Slenderness

A range of section slenderness was considered by varying the thickness of steel faceplates while keeping the overall dimensions constant. The effective stress-strain model for steel was used for non-compact and slender sections, to account for local buckling of steel. The obtained critical load against slenderness plots are shown in Figure 4.2, which has plots for 400 °C and 900 °C with the curves identified by section slenderness and temperature in the legend.

Section slenderness has a significant effect on the critical load. The critical load decreased by nearly 40% for a non-compact section compared to a compact section. This is because local buckling for non-compact and slender sections prevents the steel from achieving its full yield strength. Thus, the column fails at lower axial loads. However, the effect of section slenderness decreases with increasing surface temperature, as the plots for 900°C are nearly coinciding. This is due to steel carrying lower fraction of the axial loads at higher temperatures, minimizing the effect of local buckling on overall capacity.

#### 4.1.3. Steel Yield Strength

Steel yield strength was ranged from 358 MPa to 482 MPa to study its effect on column behavior. The results from these models are shown in Figure 4.3, the plots identified by steel yield strength and temperature in the legend.

The figure shows that steel yield strength does not significantly affect the load capacity of CFTs. The capacity of columns increased slightly at 400°C by increasing steel strength. However, the effect of steel yield strength was negligible at 900°C and the results were close. This occurred due to strength degradation of steel at high temperatures, which resulted in concrete resisting most of the applied axial load.

#### 4.1.4. Concrete Compressive Strength

Concrete compressive strength ( $f'_c$ ) was varied from 27 MPa to 48 MPa, to study its effect on column capacity. The obtained results are compared in Figure 4.4. The plots are identified by concrete compressive strength and surface temperature in the legend.

Figure 4.4 shows that the load capacity of CFTs increases with increasing concrete compressive strength for a surface temperature of 400 °C. However, the capacity shows a smaller increase when the surface temperature is 900 °C. Concrete compressive strength has a significant influence on the CFT capacity as most of the concrete remains at relatively low temperatures due to its low thermal conductivity. At elevated temperatures, concrete resists most of the applied axial load and changing its strength affects column capacity.

### 4.2. Effect of Fire Protection

As the next step of CFT analysis, studies were conducted to analyze the effect of fire protection on CFT column behavior. Applying a layer of fire protection is a common practice in the industry to increase the fire resistance of structural components. The fiber model was developed to simulate the effect of a layer of fire protection on the steel surface. The fire protection used in this study was a 4 mm thick layer of gypsum with specific heat capacity  $C = 1047 \text{ J/(kg K)}$  and thermal conductivity  $k = 0.120 \text{ W/(m K)}$ . The column was a 300mm x 300mm square section with 6mm thick steel faceplates. Steel with a yield strength of 358 MPa and concrete with

compressive strength 38MPa was considered. The results are presented in a plot of critical load against slenderness for different steel surface temperatures, similar to the parametric study in 4.1.

Figure 4.5 shows the comparison of critical load against slenderness for steel surface temperatures of 400 °C and 700 °C for the column with and without fire protection. For a given temperature and slenderness ratio, the column with fire protection has a lower load capacity compared to the column without fire protection. This is because, for a given steel surface temperature, concrete is at a higher average temperature in the column with fire protection due to a shallower temperature gradient. For the column with fire protection, there is a temperature drop across the layer of fire protection which is not accounted for, meaning steel is at a lower temperature compared to the surrounding gas temperature. Figure 4.6 shows this comparison of temperature profiles across the section when the steel surface is at 600 °C. In the plot, concrete elements are at higher temperatures in the specimen with fire protection.

The effect of fire protection on steel surface temperature and fire resistance (time to failure) of CFTs is shown in Figure 4.7. Axial displacement against steel surface temperature and time is plotted in this figure for the two columns (with and without fire protection). Figure 4.7(a) shows that axial displacements have the same trends and maximum values in both cases, but steel gets heated to ~1000°C in the absence of fire protection compared to ~700°C with fire protection. Similarly, Figure 4.7(b) shows that application of fire protection increases the time to failure by nearly 2.5 times. This is because fire protection significantly delays the heating of steel and restricts steel to temperature around 700°C.

### 4.3. Concrete Contribution Factor to Stiffness

The variation of concrete contribution to effective stiffness of a CFT column is discussed in this section. As per AISC 360 (2016), the effective stiffness of filled composite axial members at ambient temperature is given by Eqn. 4.1a. In this equation, the factor  $C_3$  accounts for cracking of concrete, as cracked concrete is assumed not to contribute to effective stiffness.

$$(EI)_{eff} = E_s I_s + C_3 E_c I_c \quad (4.1a)$$

$$C_3 = 0.45 + 3 \left( \frac{A_s}{A_g} \right) \leq 0.9 \quad (4.1b)$$

where,

$A_s$ : area of steel faceplates

$A_g$ : gross section area

$E_s$ : modulus of elasticity of steel

$E_c$ : modulus of elasticity of concrete

$I_s$ : moment of inertia of steel about the section centroid

$I_c$ : moment of inertia of concrete about the section centroid

From Eqn. 4.1b, it is evident that  $C_3$  is a function of section slenderness. This study investigated the validity of this formula at elevated temperatures using the fiber model. The contribution factor was calculated at failure as the ratio of effective stiffness ( $EI$ ) of uncracked concrete elements to the total concrete elements, as given in Eqn. 4.2.

$$C_3 = \frac{\sum_{compression} E_c(T)I_c}{\sum_{uncracked} E_c(T)I_c} \quad (4.2)$$

In Eqn. 4.2, the modulus of elasticity for each element was taken as a function of its temperature according to the values given in Table A-4.2.2 of AISC (2016). Moment of inertia for each element was calculated about the section centroid. A square CFT column with overall dimensions of 300mm x 300mm was taken as the column which was analyzed with varying section slenderness, axial load and column slenderness. The axial load was maintained at 20%, 40% and 60% of the ambient nominal capacity (AISC, 2016: Chapter I) for each case. The obtained results are plotted in Figure 4.8. The graphs show the variation of  $C_3$  with cross section slenderness for different axial loads. The graphs are plotted for section aspect ratio of 1 and 2 and column slenderness of 5 and 15.

It is evident from Figure 4.8 that  $C_3$  decreases with increasing cross section slenderness, approaching a constant value of 0.45. Also, at elevated temperatures,  $C_3$  is a function of the axial load and column slenderness. As the applied axial load increases, there is a higher net compressive stress in the column and more concrete is uncracked as it is in compression. Comparing with the AISC (2016) recommended curves, it is observed that the AISC (2016) recommended equation is conservative for axial loads greater than 50% of the nominal capacity, but it gets unconservative for high section slenderness and low axial loads. A modified equation to estimate  $C_3$  could be

proposed for elevated temperatures. The need for a modified equation is further covered in the next section.

#### 4.4. Capacity Prediction Equation for CFTs at Elevated Temperature

Based on the observations discussed in the previous sections and the results of the parametric study, a set of equations to predict the capacity of CFTs at elevated temperatures was developed and proposed, which is discussed here. For this purpose, the results from the parametric study were normalized to be plotted on a single graph.

The experimental critical load [ $P_{cr}(T)$ ], which is the axial load applied on the CFT column for each iteration, was normalized to the calculated nominal axial compressive strength (zero length) of the column at the failure time [ $P_{no}(T)$ ]. This nominal capacity was calculated based on the steel surface temperature and the temperature of all the concrete elements (at failure). This non-dimensional ratio [ $P_{cr}(T)/ P_{no}(T)$ ] was plotted on the y-axis. The equations used for its calculation are given as follows:

For compact sections ( $\lambda < \lambda_p$ ),

$$P_{no}(T) = A_s F_y(T) + 0.85 \sum_{i=elements} f'_c(T_i) A_{ci} \quad (4.3)$$

For non-compact sections ( $\lambda_p < \lambda < \lambda_r$ ),

$$P_{no}(T) = P_p - \frac{P_p - P_y}{\lambda_r - \lambda_p} (\lambda - \lambda_p)^2 \quad (4.4a)$$

$$\text{Where } P_p(T) = A_s F_y(T) + 0.7 \sum_{i=elements} f'_c(T_i) A_{ci} \quad (4.4b)$$

For slender sections ( $\lambda > \lambda_r$ ),

$$P_{no}(T) = A_s F_{cr}(T) + 0.7 \sum_{i=elements} f'_c(T_i) A_{ci} \quad (4.5a)$$

$$\text{Where } F_{cr}(T) = \frac{9E_s(T)}{\left(\frac{b}{t_s}\right)^2} \quad (4.5b)$$

In these equations, slenderness ratio ( $\lambda$ ) is defined as ( $b/t_s$ ) where  $b$  and  $t_s$  are the larger column dimension and steel faceplate thickness, respectively.  $A_s$  is the cross-sectional area of steel

faceplates and  $F_y(T)$  is the yield strength of steel at failure surface temperature. For concrete, summation was carried out over all concrete elements where  $f'_c(T)$  is the compressive strength for the given element temperature and  $A_{ci}$  is the area of that element. Steel and concrete strengths as a function of temperature were calculated from Tables A-4.2.1 and A-4.2.2 of AISC (2016). This normalized critical load is plotted against the ratio of  $[P_{no}(T)]$  to elastic buckling strength  $[P_e(T)]$  at the failure temperature  $[P_{no}(T)/P_e(T)]$  on the x-axis. The elastic buckling strength at failure temperature is calculated as follows:

$$P_e(T) = \frac{\pi^2 EI_{eff}(T)}{(L_c)^2} \quad (4.6a)$$

$$EI_{eff}(T) = E_s(T)I_s + C_3 \sum_{i=elements} E_c(T_i)I_{ci} \quad (4.6b)$$

Where  $EI_{eff}(T)$  is the effective section stiffness, which is calculated using Eqn. 4.6b.  $L_c$  is the effective length of the column, which depends on the boundary conditions.  $E_s(T)$  is the steel modulus of elasticity at failure surface temperature, and  $E_c(T_i)$  is the modulus of elasticity of concrete elements based on the associated temperature at failure.  $I_s$  and  $I_c$  are the moments of inertia of steel and concrete sections respectively, calculated about the centroid of the section.  $C_3$  is the concrete contribution factor to stiffness, which was discussed in the previous section and is calculated using Eqn. 4.1b. Based on the data points, curve-fitting was done to obtain a lower-bound curve, a median curve and a simplified bi-linear curve. These equations are given as follows:

$$\text{Lower bound: } P_{cr}(T) = P_{no}(T) \left[ 0.54 \left( \frac{P_{no}(T)}{P_e(T)} \right)^{0.3} \right] \quad (4.7)$$

$$\text{Median: } P_{cr}(T) = P_{no}(T) \left[ 0.80 \left( \frac{P_{no}(T)}{P_e(T)} \right)^{0.8} \right] \quad (4.8)$$

Simplified bi-linear:

$$P_{cr}(T) = P_{no}(T) \left[ 1 - 0.4 \left( \frac{P_{no}(T)}{P_e(T)} \right) \right] \quad \text{if } \frac{P_{no}(T)}{P_e(T)} < 1 \quad (4.9a)$$

$$P_{cr}(T) = 0.05 P_{no}(T) \left[ 13 - \frac{P_{no}(T)}{P_e(T)} \right] \quad \text{if } \frac{P_{no}(T)}{P_e(T)} \geq 1 \quad (4.9b)$$

Where  $P_{no}(T)$  is the nominal axial compressive strength (zero length) of the column at failure time, calculated as given in equations 4.3 to 4.5 and  $P_e(T)$  is the elastic buckling strength of the column at failure time which is calculated using Eqn. 4.6. Plotting the equations on the normalized plot discussed here, they can be reduced to  $y = C_1 x^{C_2}$ . Figure 4.9 plots all the experimental normalized data points, and the proposed design curves.

The lower-bound curve is significantly conservative in predicting CFT capacity comparing to the fiber model results as shown in Figure 4.9. This equation can be used to estimate the axial load capacity of CFTs, given its properties and the targeted fire resistance rating. A 2D heat transfer needs to be conducted up to the required time (fire rating). Based on the steel and concrete temperatures obtained,  $P_{no}(T)$  and  $P_e(T)$  can be calculated. The lower bound critical load can then be obtained using Eqn. 4.7.

A modified equation for  $C_3$  was not proposed in the study as the proposed design curves were seen to be conservative. This was done to simplify the calculation process, as any over-estimation of  $C_3$  was compensated by the proposed capacity equations, which are conservative.

Table 4.1: Parametric study matrix for CFTs at elevated temperature

<b>Nomenclature</b>	<b>Cross Section Dimensions (mm x mm)</b>	<b>Aspect Ratio</b>	<b>Steel Tube Thickness (mm)</b>	<b>C/S Slender-ness</b>	<b>Steel Yield Strength-Fy (MPa)</b>	<b>Concrete Compressive Strength-fc' (MPa)</b>
C-1.0-50-358-38	300 x 300	1	6	50	358	38
C-1.5-50-358-38	250 x 360	1.5	7.2	50	358	38
C-2.0-50-358-38	210 x 420	2	8.4	50	358	38
C-1.0-33-358-38	300 x 300	1	9	33	358	38
C-1.0-50-358-38	300 x 300	1	6	50	358	38
C-1.0-66-358-38	300 x 300	1	4.5	66	358	38
C-1.0-100-358-38	300 x 300	1	3	100	358	38
C-1.0-50-358-38	300 x 300	1	6	50	358	38
C-1.0-50-413-38	300 x 300	1	6	50	413	38
C-1.0-50-482-38	300 x 300	1	6	50	482	38
C-1.0-50-358-27	300 x 300	1	6	50	358	27
C-1.0-50-358-38	300 x 300	1	6	50	358	38
C-1.0-50-358-48	300 x 300	1	6	50	358	48

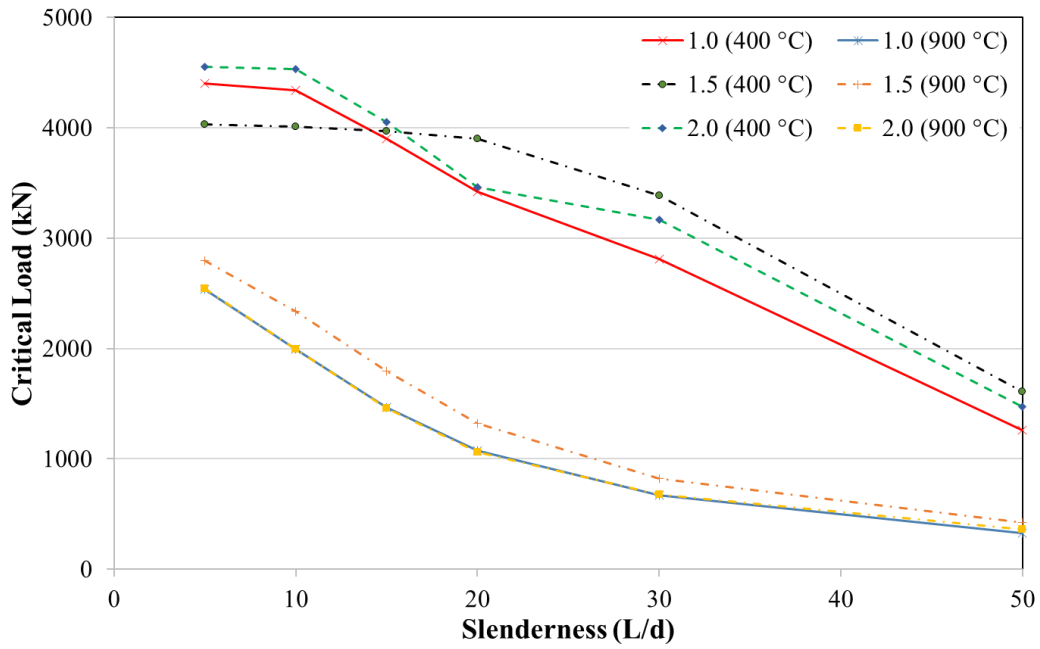


Figure 4.1: Critical load versus slenderness at two surface temperatures for various aspect ratios

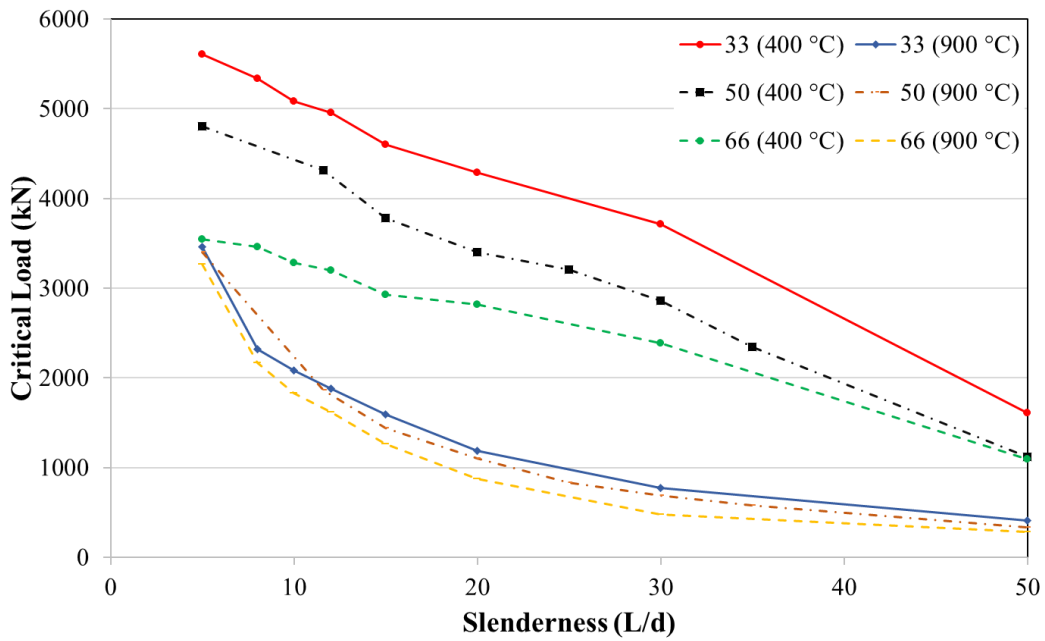


Figure 4.2: Critical load versus slenderness curves at two surface temperatures for varying section slenderness (reinforcement ratio)

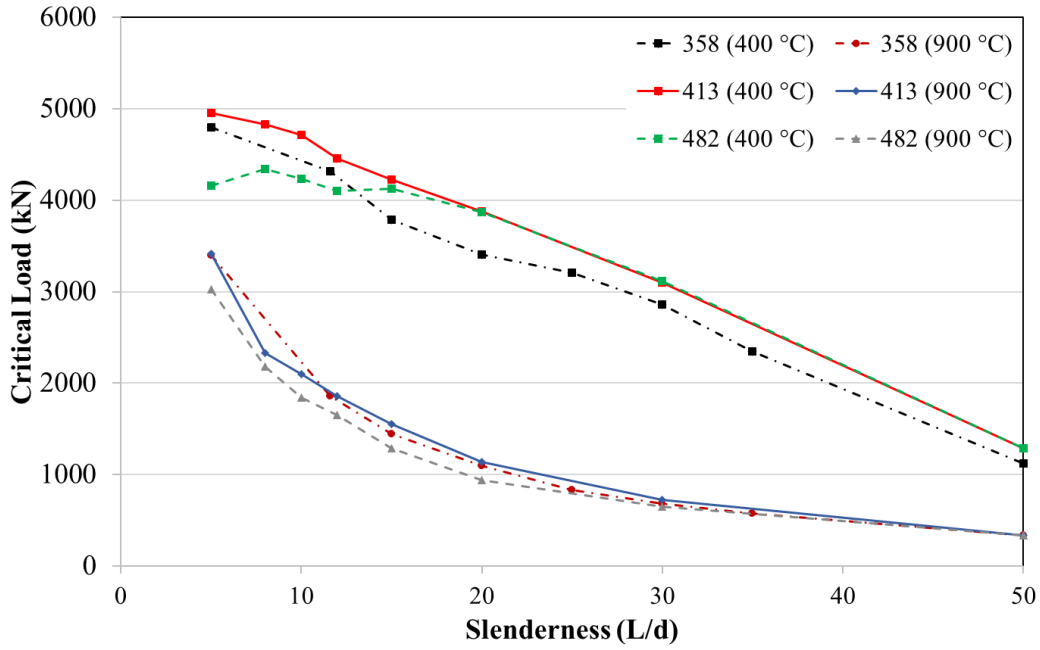


Figure 4.3: Critical load versus slenderness curves at two surface temperatures for varying steel yield strength

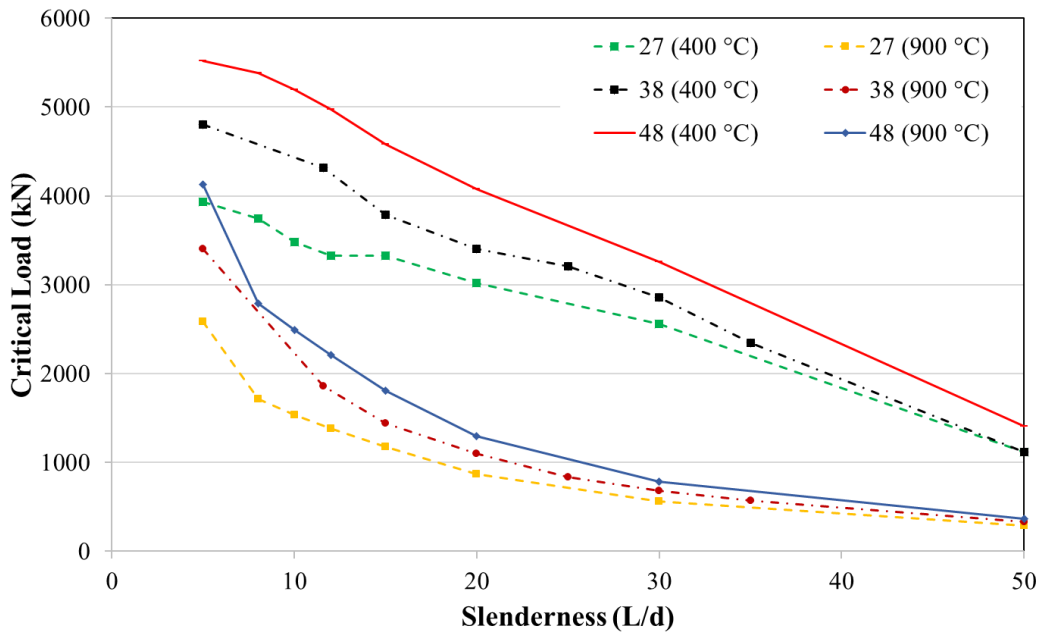


Figure 4.4: Critical load versus slenderness curves at two surface temperatures for varying concrete compressive strength

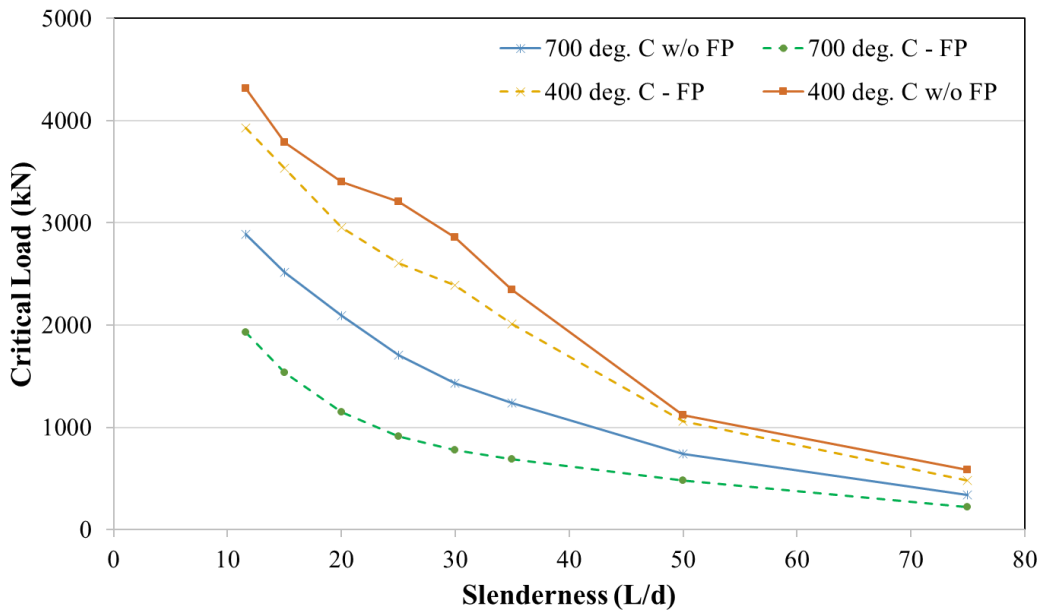


Figure 4.5: Critical load vs Slenderness comparison for two steel surface temperatures for a column with and without fire protection

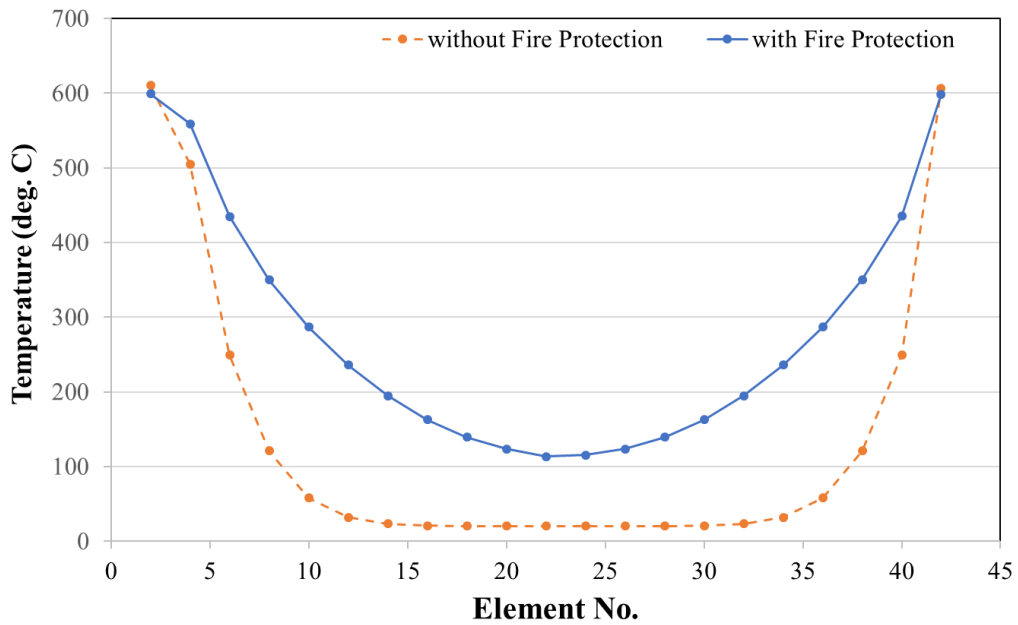
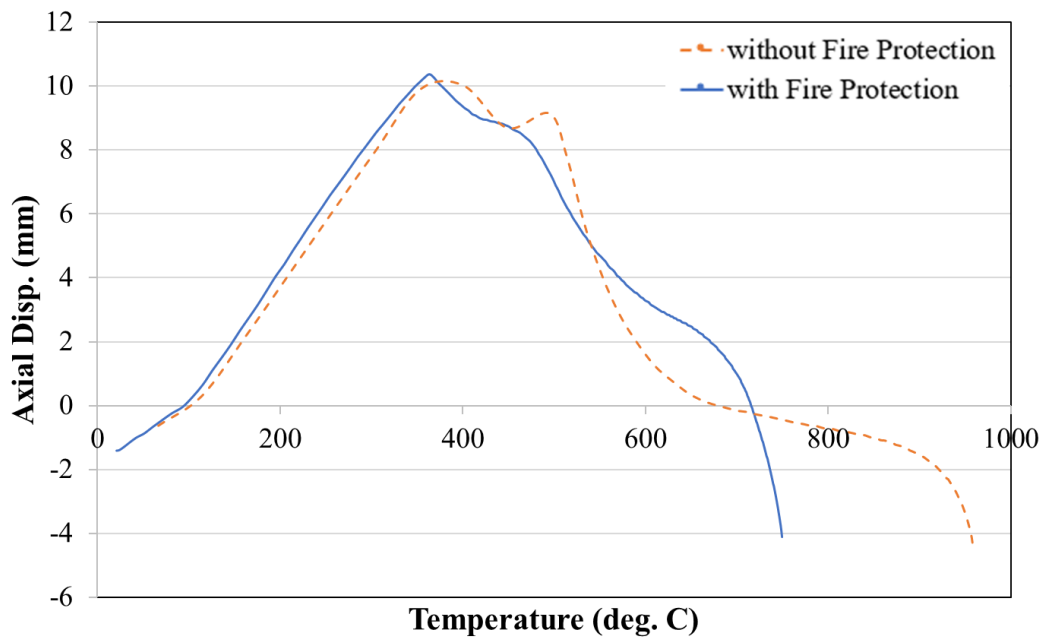
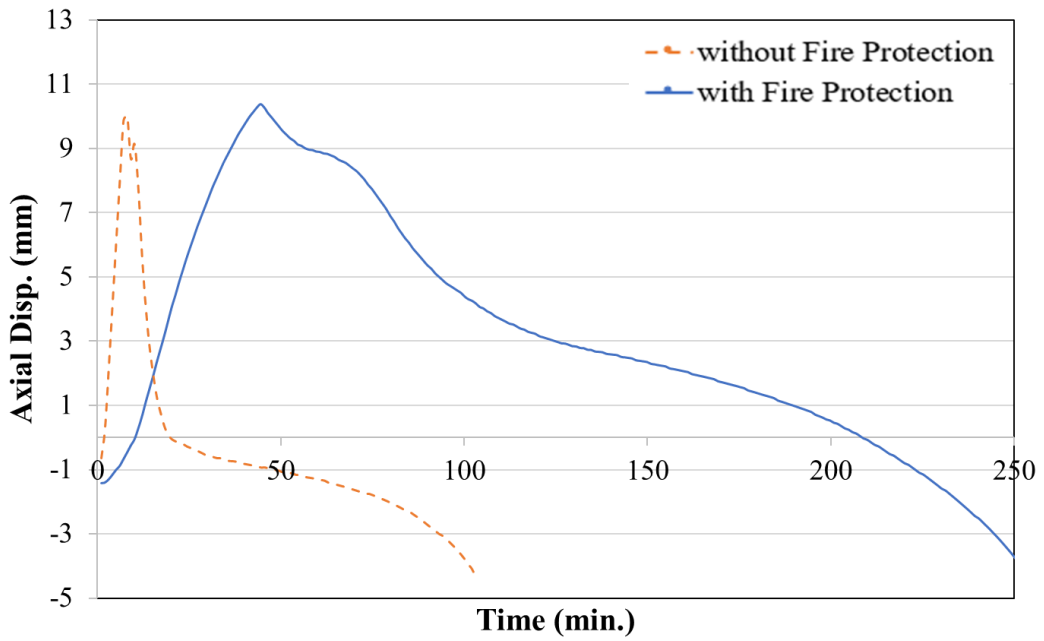


Figure 4.6: Temperature profiles for a column at failure with and without fire protection for steel surface temperature = 600 °C

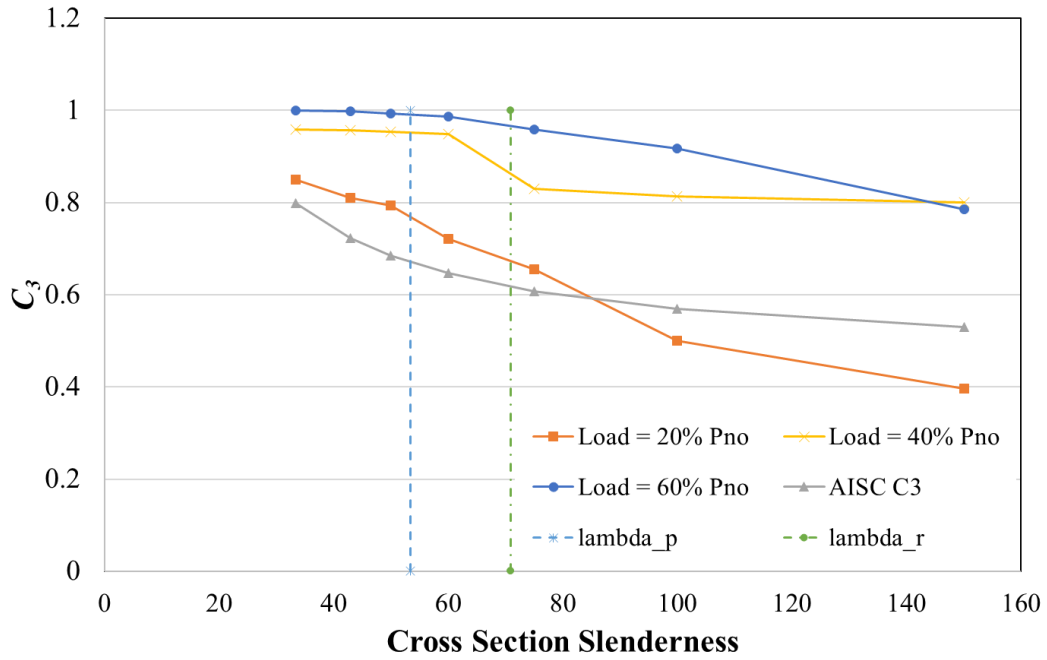


(a)

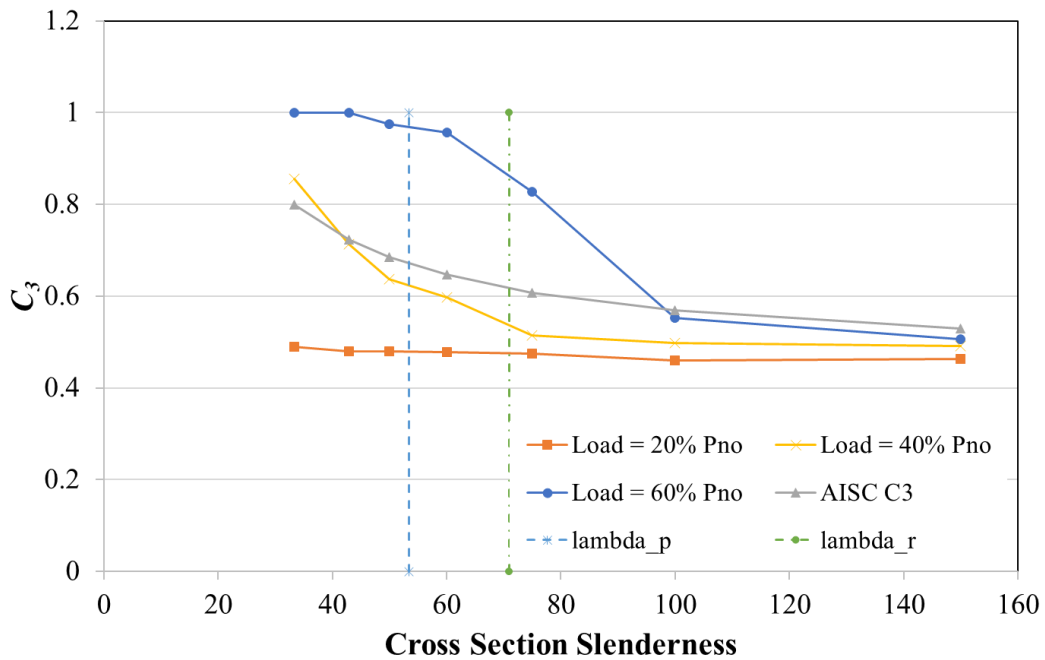


(b)

Figure 4.7: (a) Axial displacement vs surface temperature and (b) axial displacement vs time comparisons for a column with and without fire protection



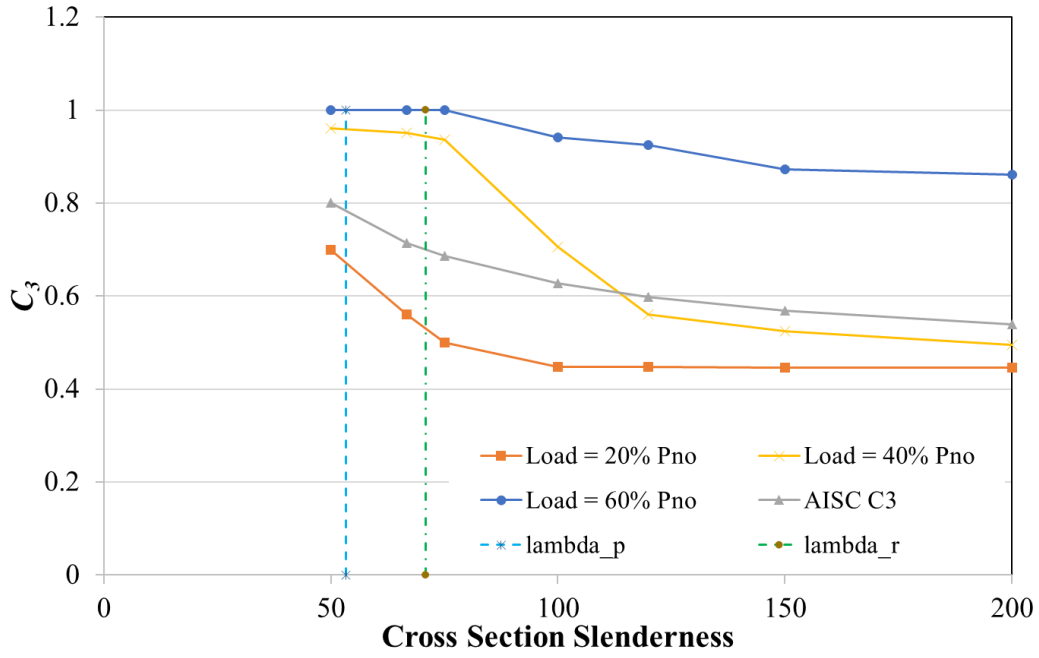
(a)



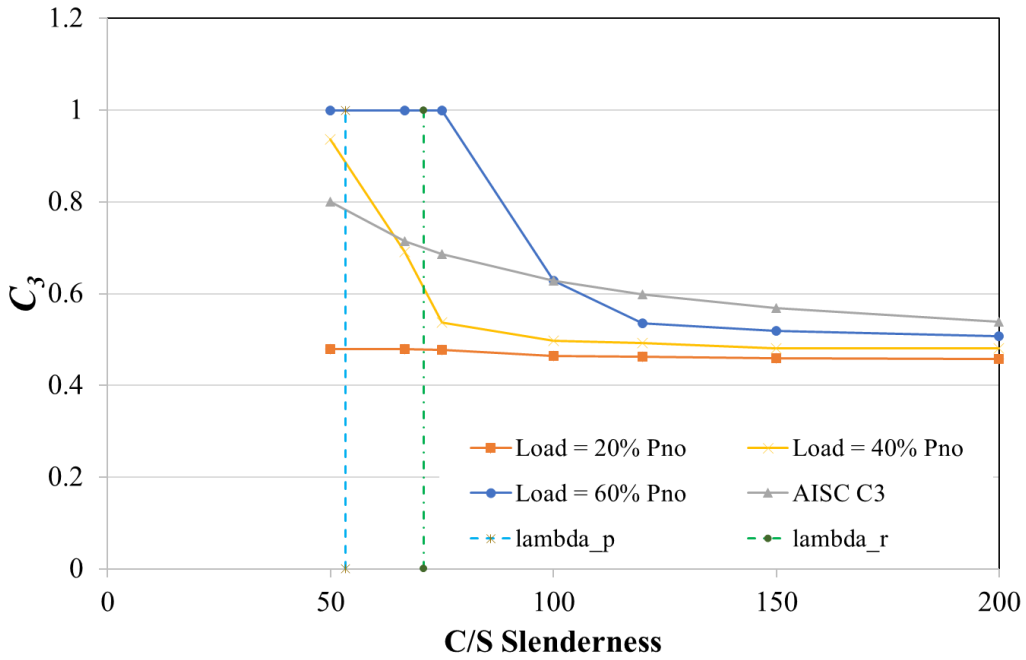
(b)

Figure 4.8: Variation of concrete contribution factor to stiffness ( $C_3$ ) with section slenderness and axial load for (a) aspect ratio = 1 & column slenderness = 5, (b) aspect ratio = 1 & column slenderness = 15, (c) aspect ratio = 2 & column slenderness = 5, (d) aspect ratio = 2 & column slenderness = 15

Figure 4.8 (continued)



(c)



(d)

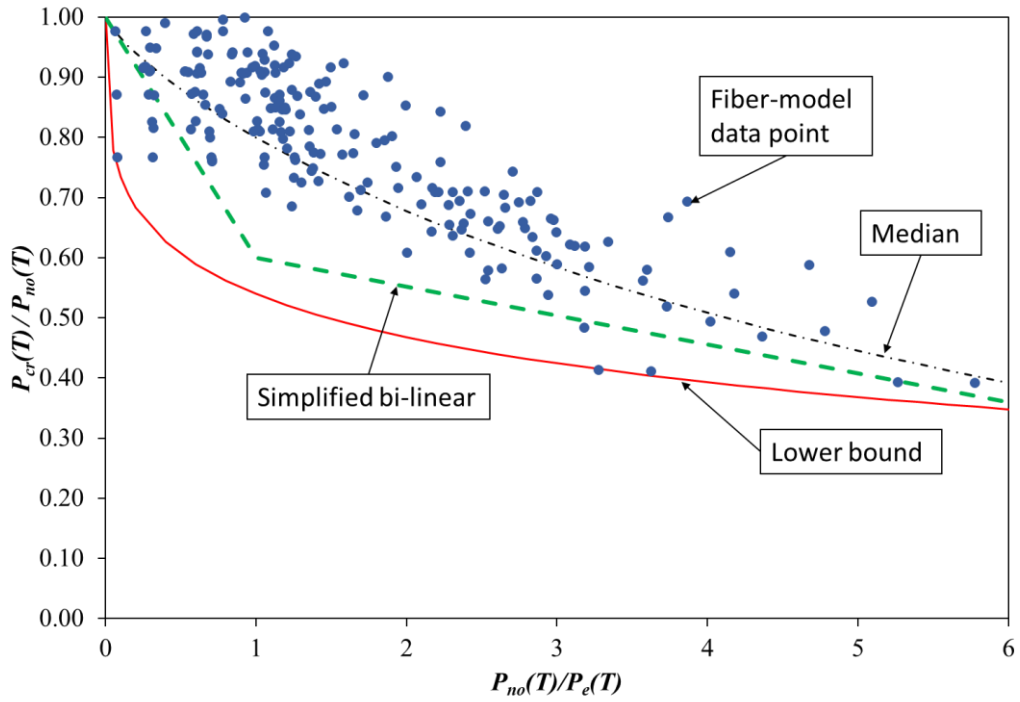


Figure 4.9: Normalized results of the parametric studies plotted with the proposed theoretical capacity curves (lower-bound, median and simplified bi-linear)

## 5. C-PSW/CF MODELING AND ANALYSIS

In the last step of this study, concrete-filled composite-plate shear walls (C-PSWs/CF) were modeled using the fiber-based tool. The objective of this analysis was to compare the performance of C-PSWs with results obtained from finite-element models and validate their behavior. For this purpose, wall specimens with varying parameters such as wall thickness, overall slenderness and applied load were compared. The details of the wall specimens used in the study are given in Table 5.1. The results of 3D finite-element modeling of these specimens were taken from Taghipour Anvari et al. (2020a).

To develop a better understanding of wall behavior, two different modeling techniques were used for walls, which were: (i) modeling the entire wall cross-section and (ii) modeling a strip of the wall section. The finite-element models developed for the walls also used these two techniques and the results from both these techniques were compared with the FEM results from the corresponding modeling techniques. Further explanation of these techniques and the obtained results are discussed in this chapter.

Single-sided heating of walls was also modeled using the strip method, in which only one face of the wall was assumed exposed to fire. As it can be expected to have situations where only one side of the walls is exposed to fire, the fiber-model was developed to be able to model the same. These results were also compared with finite-element data.

### 5.1. Section-based Models

In this modeling technique, the entire wall cross-section is modeled. As discussed previously, ties and shear studs are not modeled as the fiber model cannot account for them. The principle and algorithm for modeling of walls is similar to that of CFTs. While CFTs are typically square and have an aspect ratio less than 2, composite walls would have an aspect ratio typically greater than 3. While modeling C-PSWs, the wall section needs to be oriented such that its minor (weak) axis is horizontal, as the fiber model can simulate buckling only about the horizontal axis. For each specimen, the normalized wall capacity, axial displacement and section temperatures were compared. These values are compared with finite-element models benchmarked with experimental data.

The surface temperature across the wall section and steel surface temperature at failure are compared in Figure 3.9(a) and Figure 3.10 respectively. These comparisons were discussed in 3.3.2. Figure 5.1 shows the normalized critical load versus slenderness plots for all the tested specimens. They are plotted with FE results for comparison. In the plot, green data points are fiber model results while red points are FE results, and same shape corresponds to the same specimen (for example square represents CW-200-15). Both the fiber model and FEM data points are seen to follow a similar trend. However, there are differences in both the results, as both points of a same specimen are not coinciding. These discrepancies arise as a result of differences in temperature distribution (Figure 3.9), and other simplifying assumptions of the fiber model, listed in 3.4.

A capacity equation for C-PSWs/CF was proposed by Taghipour Anvari et al. (2020a), which is mentioned in Eqn. 5.1 and 5.2. The same equation was plotted in Figure 5.1 along with the data points for comparison and further validation of the equation. It is evident from the figure that all the data points are above the proposed lower bound curve, and also follow the trend highlighted by the median curve. Thus, the proposed equation is adequate and validated by the fiber model.

$$\text{Median: } P_{cr}(T) = \left[ 0.39 \left( \frac{P_{no}(T)}{P_e(T)} \right)^{0.3} \right] P_{no}(T) \quad (5.1)$$

$$\text{Lower-bound: } P_{cr}(T) = \left[ 0.32 \left( \frac{P_{no}(T)}{P_e(T)} \right)^{0.3} \right] P_{no}(T) \quad (5.2)$$

Where  $P_{no}(T)$  and  $P_e(T)$  are calculated as given in Chapter 4 (4.4).

For further comparison of C-PSW/CF performance, axial displacement versus time and axial displacement versus temperature curves obtained from the fiber model and FE models were compared. Figure 5.2(a) shows the plots for axial displacement versus time while Figure 5.2(b) shows the plots for axial displacement versus temperature for walls with 200 mm thickness (CW-200). Figure 5.3 shows these plots for the 300 mm thick wall specimens (CW-300). It is evident from the graphs that there is a reasonable agreement in FE results and the fiber model. The position of peak axial displacements nearly coincides for the fiber model and FE analysis. However, there are differences in the axial displacements, due to the simplifying assumptions made in the fiber

model. The differences in axial displacements are seen to be more significant for CW-300 specimens, indicating that fiber model and FE analysis results diverge for thicker wall sections.

The section-based modeling technique is the most direct approach to analyzing CFTs. However, it does present some discrepancies when compared to FEM data. Also, due to a lack of experimental data and finite-element models, the modeling of longer walls using the section-based technique could not be validated. It is thus not recommended to use this approach for longer walls.

## 5.2. Strip-based Models

In this modeling technique, the wall cross-section is discretized into strips of a constant width perpendicular to the wall direction. A single strip of the wall is then modeled and the behavior of that strip is considered to be representative of the behavior of the entire wall. A strip is considered to be having width equal to half the tie spacing on each side of a tie bar. Thus, the net width of the strip modeled equals the tie bar spacing. In this approach, steel faceplates are modeled only on two sides of the specimen, while the other two sides are assumed to have symmetric boundary conditions.

Heat is assumed to flow only perpendicular to the wall, as length of the wall is considered infinite. Heat transfer is done only in one direction and temperature along the wall length is assumed to be constant. The remaining analysis principles are similar to those of CFTs, the difference being that steel elements are only on two edges, instead of all four. The fiber model is designed to simulate buckling only in one direction (about the horizontal axis). Hence the symmetric boundary condition for the concrete edges is implicitly modeled, and need not be specifically accounted for.

A schematic of the wall section used in the strip approach is shown in Figure 5.4. Similar to 5.1, for each specimen, the normalized wall capacity, axial displacement and section temperatures were compared. These values are compared with FE analysis results. The temperature profile across the section is plotted and compared for the 200mm thick wall specimen in Figure 5.5. The time to failure and steel surface temperature at failure as predicted by the fiber model and FE analysis using the strip method for all the specimens are compared in Table 5.2. Bhardwaj et al. (2019b) recommended to use the surface temperature at failure as a metric to study the fire resistance of C-PSWs. The failure surface temperatures as predicted by the fiber model and FE

analysis are compared in Figure 5.6. The figure shows a close match in the predicted surface temperatures at failure.

Figure 5.7 shows the axial displacement versus time plots while Figure 5.8 shows the normalized critical load versus slenderness plots. The normalized load versus slenderness plot shows that the FE analysis is generally more conservative, as it predicts slightly lower critical loads as compared to the fiber-based approach. From Figure 5.7, it is observed that while there is a general agreement in predicted axial displacement, there are some differences in the axial displacement predicted by the fiber model and the FE analysis.

These differences in part can be explained by the difference in heat transfer algorithms. The fiber model algorithms generate slightly different temperature profiles across the section (Figure 5.6). Fiber model predicted temperatures are lower than the FE analysis beyond 200 minutes, hence the lower predicted strengths by the finite-element models can be explained. The simplifying assumptions of the fiber model (3.4) would also explain the differences.

Similar to the section method, the proposed capacity equations for C-PSWs/CF (Eqn. 5.1 & 5.2) are plotted on the normalized load versus slenderness plot (Figure 5.8), to validate these equations using the fiber model. The proposed lower-bound equation is sufficiently conservative when compared to the fiber model results. Hence, the proposed curve can be used to estimate wall capacity.

The results from section method and strip method for the fiber model were compared, to determine the appropriate approach for modeling of wall sections. This comparison was done in terms of the normalized critical load versus slenderness data points. Figure 5.9 shows this comparison where data points from both methods are plotted together on the normalized load versus slenderness plot. The plot shows that the strip method is generally more conservative, as its data points are lower on the curve. This is because the strip-based method ignores the effect of boundary elements (flange plates, cover plates) of the wall. Further, it is evident from Figure 5.8 that the strip-based method gives results which are more consistent with FE analysis compared to the section-based approach. Also, considering that the strip method is independent of the length of the wall, it is recommended to be used for modeling C-PSWs/CF.

### 5.3. Single-sided Heating: Strip-based Approach

As the last step of the study, single-sided heating of C-PSWs/CF was modeled. In this study, fire was assumed to be present only on one side of the wall. Only one face of the wall was exposed to fire loading while the other face remained at ambient temperature. Such a fire scenario can occur where there is fire on one side of the structure, exposing only one face of walls to fire. The fiber-model was designed to be able to model single-sided heating for walls using the strip-based approach.

Heat transfer was modeled in one direction, perpendicular to the length of the wall. The unexposed face of the wall was assumed to remain at room temperature (20 °C). Heat loss to the atmosphere through the unexposed face was calibrated by adjusting the value of convection coefficient. The variation of temperature across the wall thickness was compared with FE analysis and is shown in Figure 5.10. The graph shows the temperature at various nodes across the section at different time instants as obtained from the fiber model and FE analysis. There is a good agreement in the temperature profiles obtained from the two models.

Further steps of analysis involve developing a cross-section moment-curvature curve for the calculated temperature states. Newmark's modified method is implemented to obtain a converged deflected shape, as outlined in 3.1. As material stiffness of steel and concrete reduces with increasing temperatures, center of stiffness of the section will vary with time for non-symmetric heating. Hence center of stiffness of the section and load eccentricity are calculated at each time step, and the primary moment due to eccentricity is updated in modified Newmark's method. Lateral displacement and curvature in the direction of the heated face are taken as positive. A comparison of out-of-plane displacements obtained from the fiber model and FE analysis for the CW-300-10 strip model is shown in Figure 5.11. The graph shows the variation of out-of-plane displacement against the temperature of the steel surface exposed to fire. There is a good agreement in the displacements, with both the models predicting comparable peak out-of-plane displacement.

Wall sections with varying height (wall slenderness) were modeled for single-sided fire to study the effect of height on the direction of global buckling. A wall section with overall thickness 300 mm, width of 150 mm and steel faceplate thickness of 6 mm was modeled. Steel and concrete strengths were taken as 345 MPa and 40 MPa respectively. Axial load equal to 20% of  $A_g f'_c$  was applied. Wall sections with overall slenderness of 10, 15, 20, 22, 25 and 30 were considered. Figure

5.12 plots the out-of-plane displacement for the six models against temperature of the exposed steel surface.

All the walls were observed to initially buckle in the positive direction (direction of heated face). This is because of thermal moments due to asymmetric heating which cause the heated steel faceplate to expand while the remaining section remains at its original length. The shorter walls ( $L/d < 20$ ) were seen to buckle in the opposite direction (towards the unexposed face) after a period of heating. The asymmetric heat resulted in steel and concrete near the exposed face losing more stiffness compared to the material near the unexposed face. Center of stiffness thus shifted towards the unexposed face. As load was assumed to act at the geometric center of the section, a primary moment was generated which was opposite to the moments imposed due to the expansion of material on the heated face (thermal moments). A representation of the two types of moments generated is shown in Figure 5.13. The wall section buckled towards the unexposed face when the primary moment overcame the thermal moment.

Another observation from Figure 5.12 is the difference in failure surface temperature (and thus failure time) for different wall sections. Walls with slenderness greater than 20 failed at low surface temperatures (relatively smaller time to failure) while short walls were stable for longer a longer duration. This is because for high slenderness, the moments arising from the asymmetric thermal gradients were enough to cause instability even at lower temperatures. Slender wall sections were seen to fail quickly even for low applied axial loads. This is represented in Figure 5.14 which shows the failure time and temperature at failure of the exposed steel face for different applied load ratios. The graph shows the behavior of the wall section with overall slenderness of 25. Load was applied as a fraction of the ambient nominal capacity of the wall section (AISC, 2016). Even for low load ratios of 10%, the wall section failed at 41 minutes, or at a surface temperature of 725 °C. Wall sections with slenderness less than 20, however, were seen to be stable for a significantly longer duration (240 minutes to 600 minutes). Such a difference in behavior is not observed for symmetric fire loading as thermal effects do not produce any moment when a member is heated symmetrically. In such cases, moments arise only because of imperfections in the member.

The wall models were also studied for an applied load ratio of 30%  $A_g f'_c$  to understand the relative effect of applied axial load and wall slenderness. The time to failure (fire resistance) of the

six models for 20% and 30% applied axial load was plotted. This graph is shown in Figure 5.15. Fire resistance decreases rapidly as wall slenderness goes beyond 20, and it is seen to be independent of the applied load. This is as the plots for 20% and 30%  $A_g f'_c$  are nearly coinciding for  $L/d > 20$ . For wall slenderness less than 20, the applied axial load has a significant effect on fire resistance. Further, these results were plotted on the normalized load versus slenderness plot, shown in Figure 5.16. The proposed lower-bound equation (Eqn. 5.2) is also plotted for comparison. The figure shows four series of data points, with wall slenderness less than and greater than 20, and applied axial load of 20% and 30%  $A_g f'_c$ . This plot also shows that wall sections with  $L/d > 20$  are below the proposed capacity curve, hence having inadequate capacity. Shorter walls ( $L/d < 20$ ) are seen to have adequate capacity compared to the proposed design curve.

From these observations, it can be concluded that wall slenderness has a significant effect on the behavior and stability of C-PSWs under asymmetric fire loading. Slender wall sections ( $L/d > 20$ ) have a poor fire resistance (20-40 mins.) irrespective of the applied axial load. For short walls ( $L/d < 20$ ), the proposed capacity equations (Taghipour Anvari et al., 2020a) were seen to be adequate in predicting axial load capacity. It is recommended to specify slenderness limits for construction of walls that are designed for asymmetric fire loading. Based on the results of these studies, it is recommended to limit the wall slenderness, or the floor height to wall thickness ratio to 20 for steel faceplates directly exposed to asymmetric fire loading (no fire protection). For more slender walls, it is recommended to apply fire protection. Additional experimental and numerical studies are recommended to determine the dependency of wall stability on other wall parameters such as thickness, reinforcement ratio and material properties.

Table 5.1: Details of wall specimens for comparison with FE analysis (Taghipour Anvari et al., 2020a)

<b>Nomenclature</b>	<b>Height h (mm)</b>	<b>Length L(mm)</b>	<b>Thickness T (mm)</b>	<b>Steel thickness <math>t_p</math> (mm)</b>	<b>Applied Load <math>P/A_g f'_c</math></b>	<b>Slenderness h/T</b>	<b><math>2t_p/T</math></b>
CW-200-5-20	1000	600	200	4	20%	5	4.00%
CW-200-10-20	2000	600	200	4	20%	10	4.00%
CW-200-15-20	3000	600	200	4	20%	15	4.00%
CW-200-20-20	4000	600	200	4	20%	20	4.00%
CW-300-5-20	1500	900	300	6	20%	5	4.00%
CW-300-10-20	3000	900	300	6	20%	10	4.00%
CW-300-15-20	4500	900	300	6	20%	15	4.00%
CW-300-20-20	6000	900	300	6	20%	20	4.00%
CW-400-15-20	6000	1200	400	8	20%	15	4.00%
CW-400-20-20	8000	1200	400	8	20%	20	4.00%

Table 5.2: Comparison of failure time and surface temperature as predicted by fiber model and FE analysis (Taghipour Anvari et al., 2020a)

<b>Nomenclature</b>	<b>Fiber model predicted failure time (min.)</b>	<b>FEM predicted failure time (min.)</b>	<b>Fiber model predicted failure surface temperature (°C)</b>	<b>FEM predicted failure surface temperature (°C)</b>
CW-200-05-20	NF	198.2	NF	1105.3
CW-200-10-20	150.9	160.1	1050.4	1067.0
CW-200-15-20	97.5	112.1	977.2	1004.3
CW-200-20-20	69.3	81.4	905.8	942.0
CW-300-05-20	NF	352.6	NF	1197.0
CW-300-10-20	283.9	249.8	1155.1	1140.0
CW-300-15-20	174.7	140.1	1074.9	1041.5
CW-300-20-20	114.1	121.5	1003.4	1015.0
CW-400-15-20	278.5	209.3	1151.9	1110.0
CW-400-20-20	174.3	170.9	1074.5	1075.0

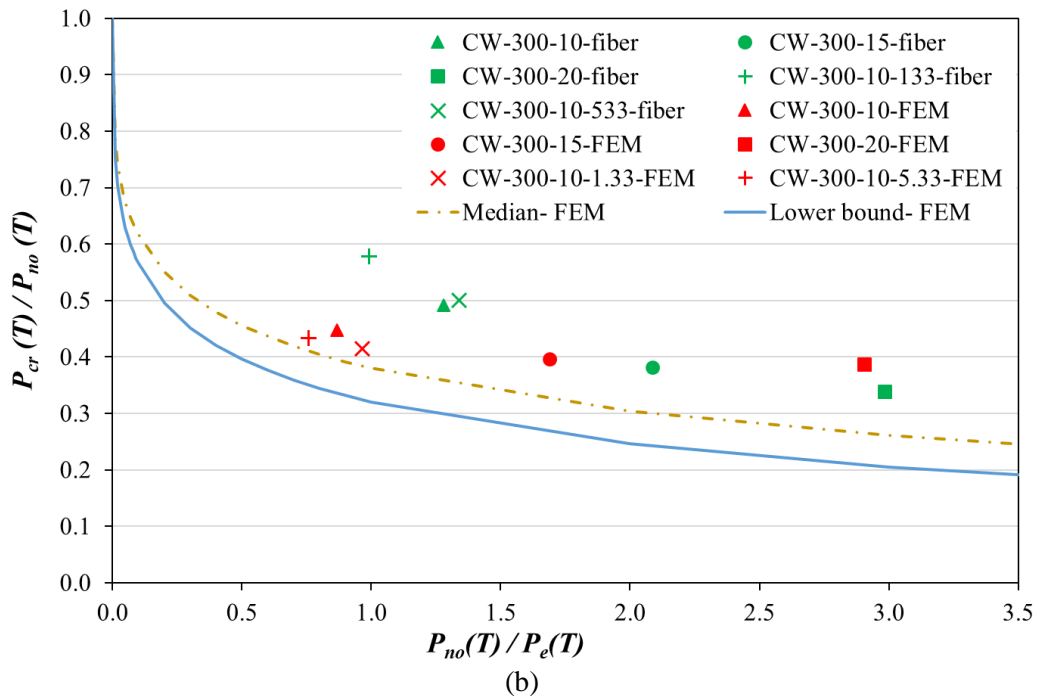
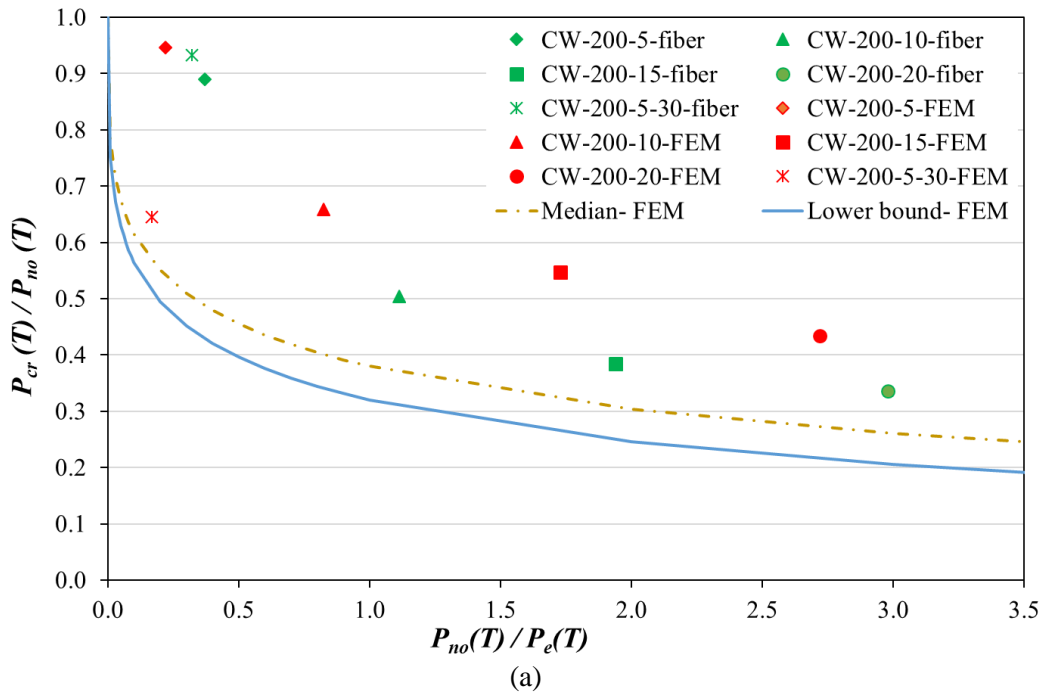
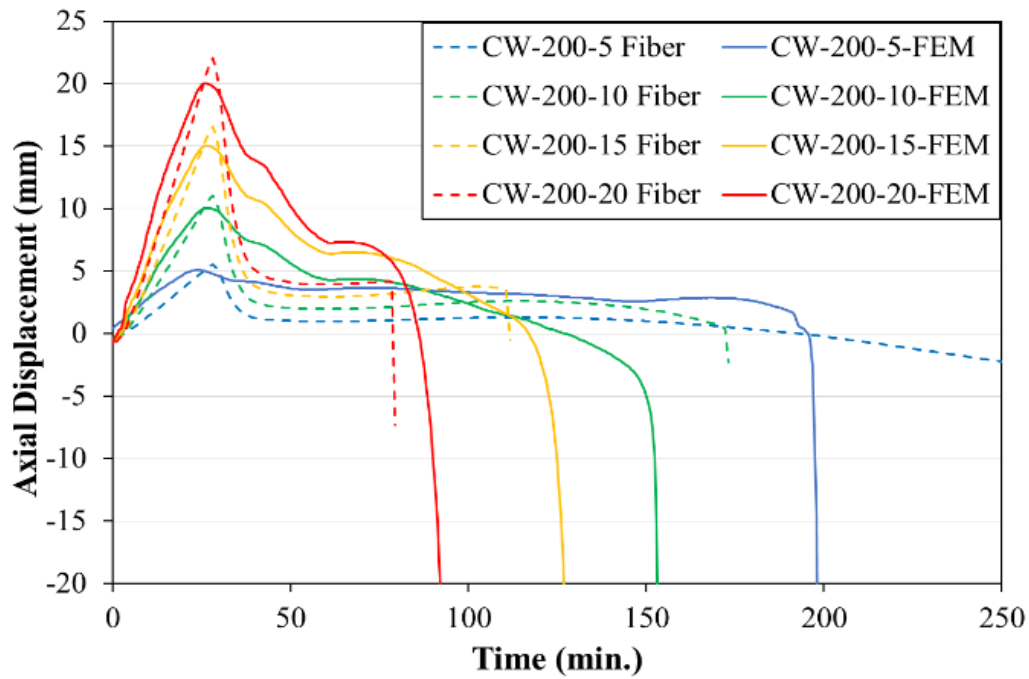
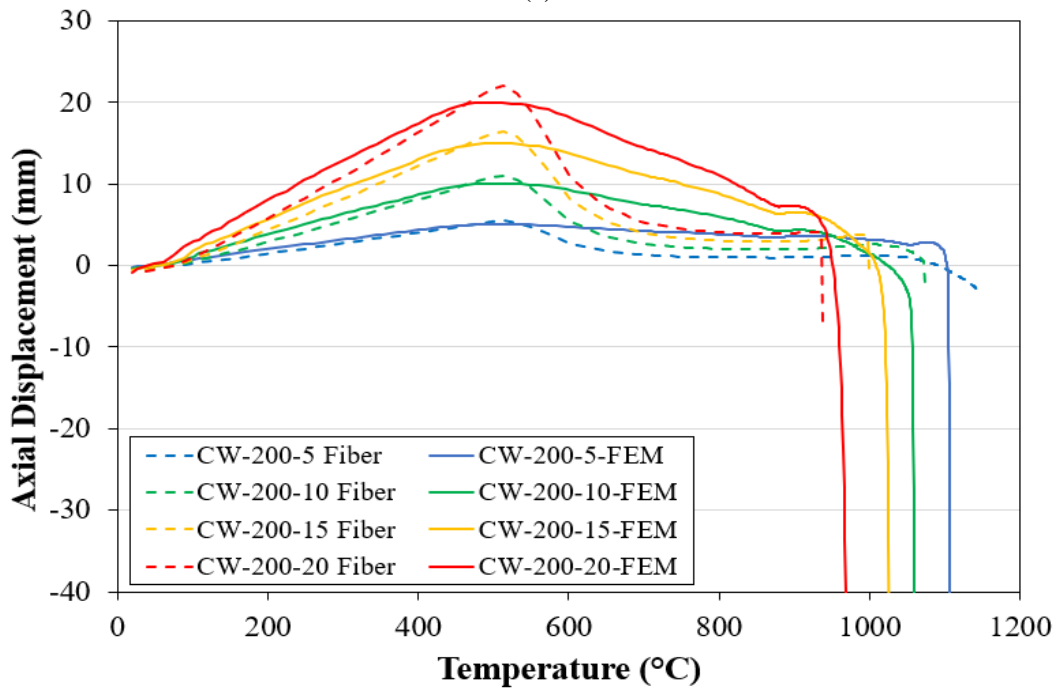


Figure 5.1: Normalized results of the comparison between fiber-model and FEM data for wall specimens using section method for (a) 200 mm wall thickness and (b) 300 mm wall thickness



(a)



(b)

Figure 5.2: Comparison of fiber-model and FE analysis predicted axial displacements for CW-200 specimens using section method; (a) axial displacement vs time and (b) axial displacement vs surface temperature

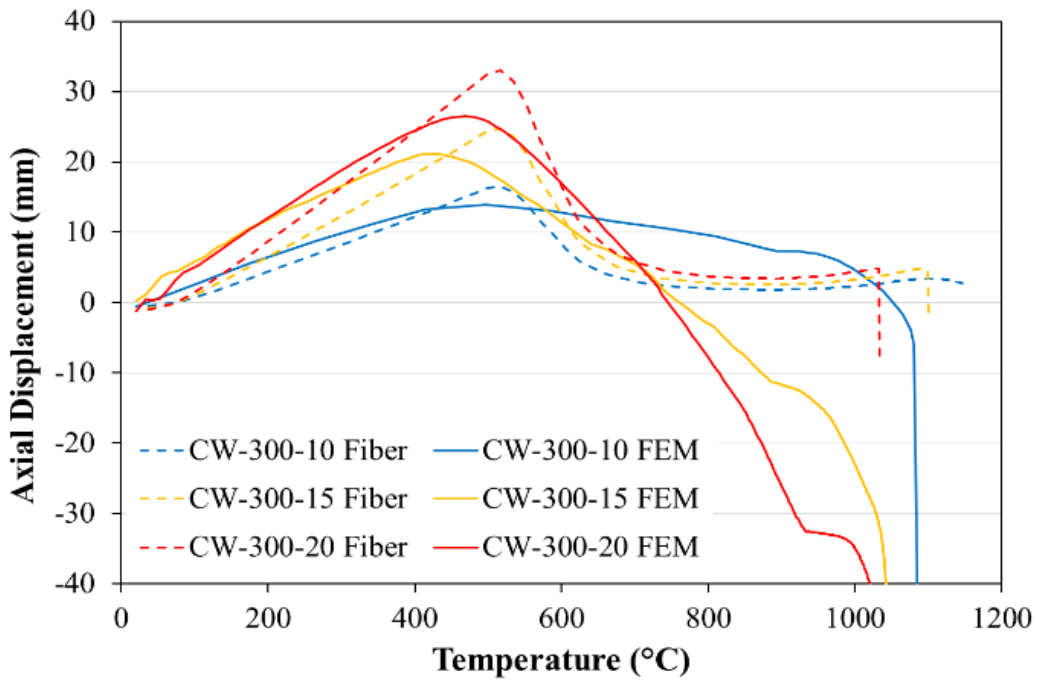
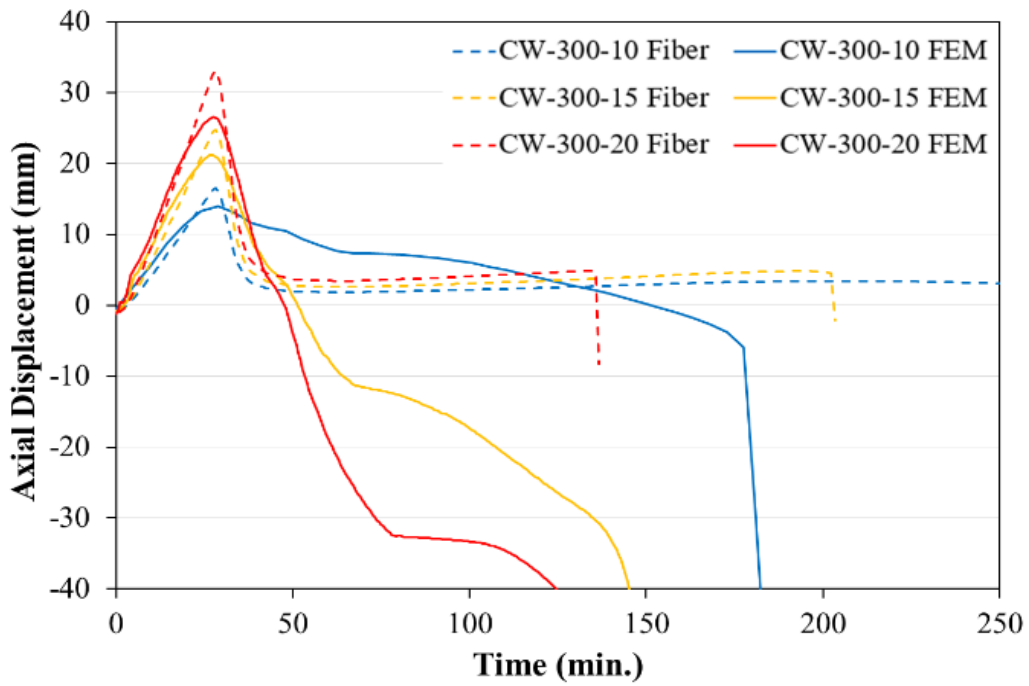


Figure 5.3: Comparison of fiber-model and FE analysis predicted axial displacements for CW-300 specimens using section method; (a) axial displacement vs time and (b) axial displacement vs surface temperature

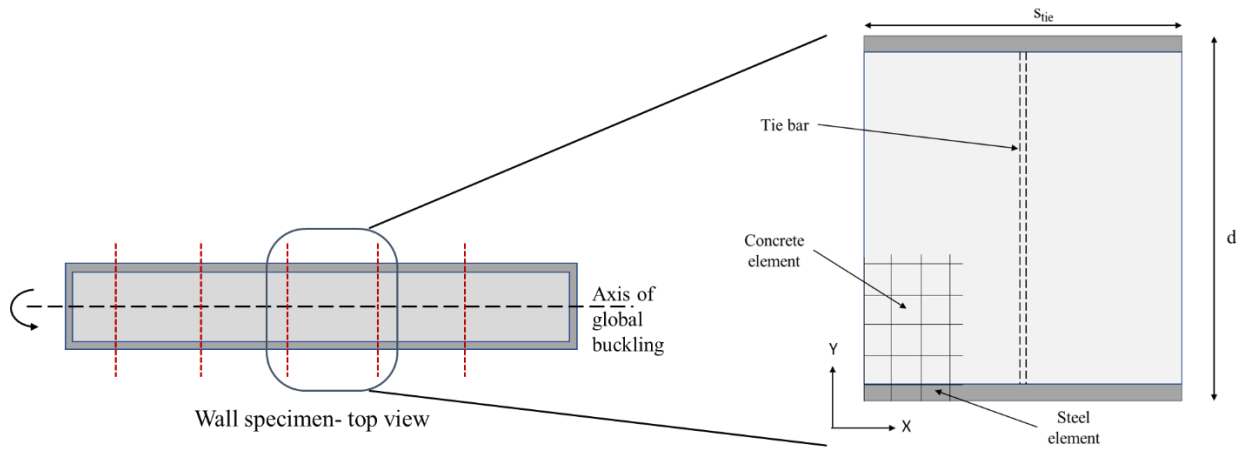


Figure 5.4: Schematic of a wall section for strip-based modeling approach

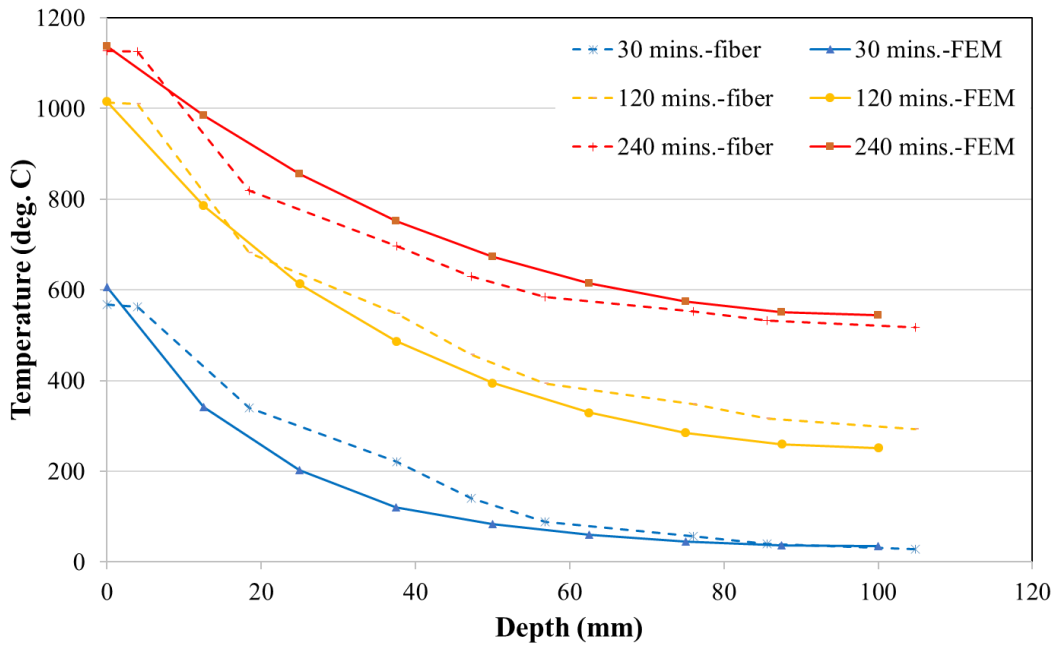


Figure 5.5: Temperature profiles comparison at three time instants for half section (CW-200) between fiber model and finite element model- strip method

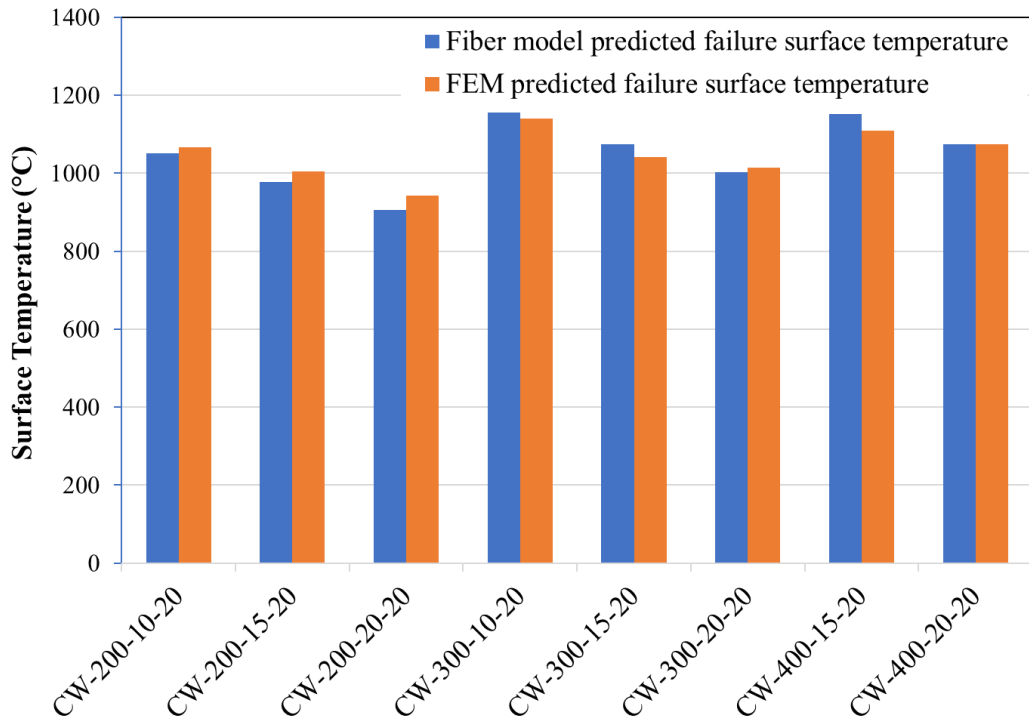
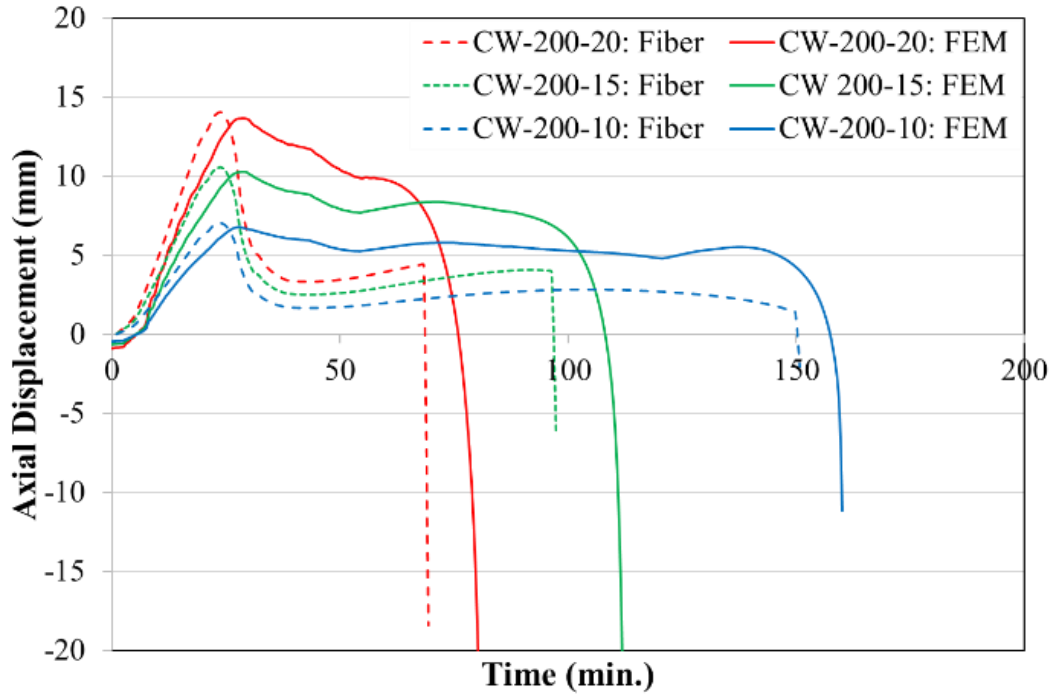
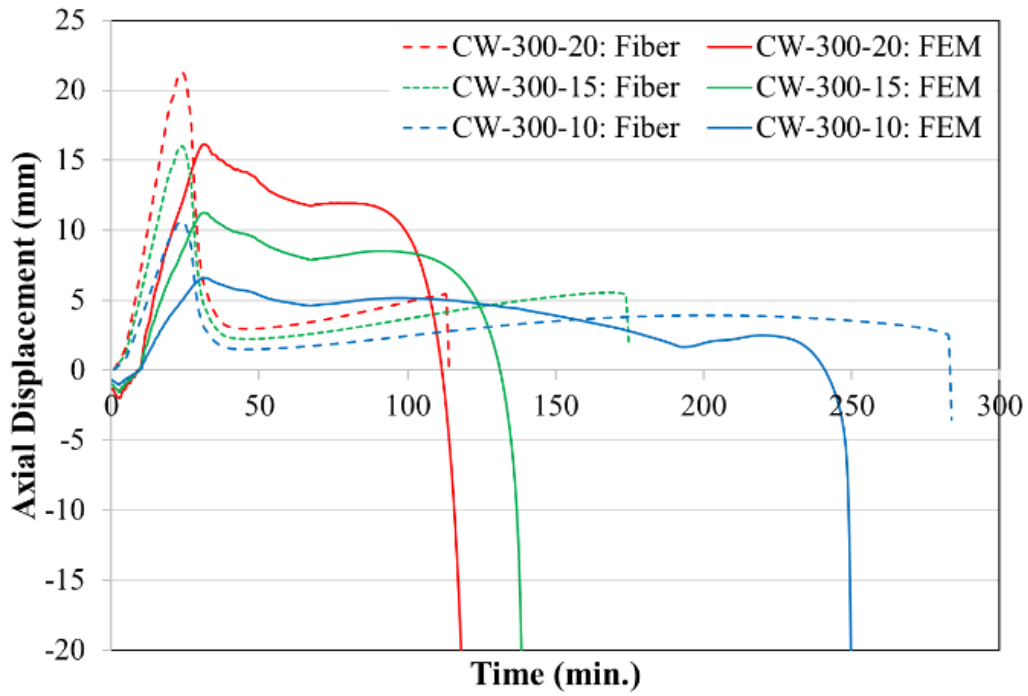


Figure 5.6: Comparison of failure surface temperatures as predicted by fiber model and FE analysis- strip method

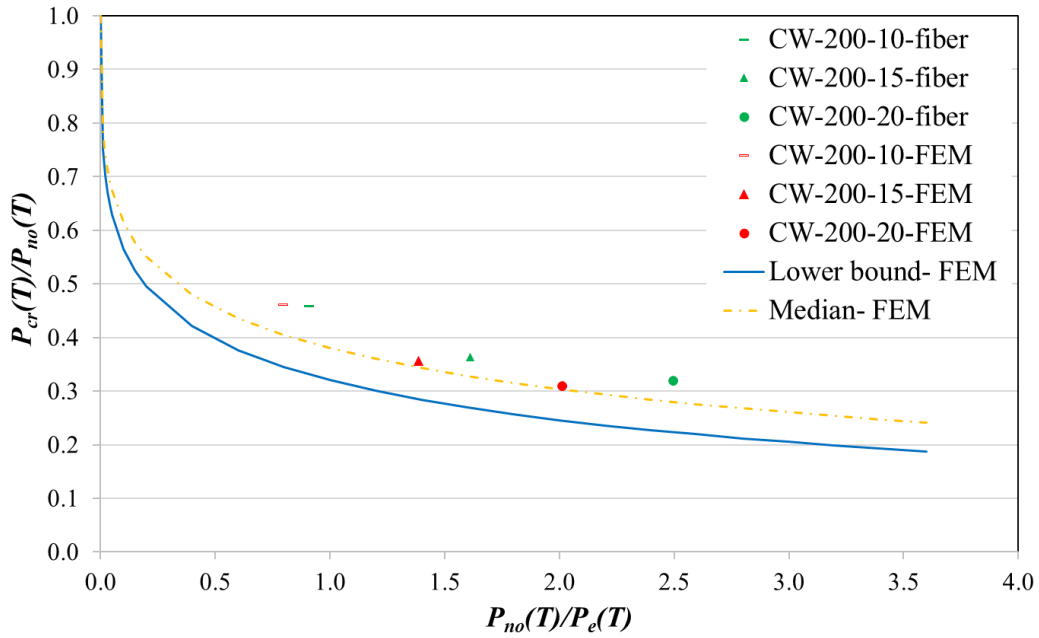


(a)

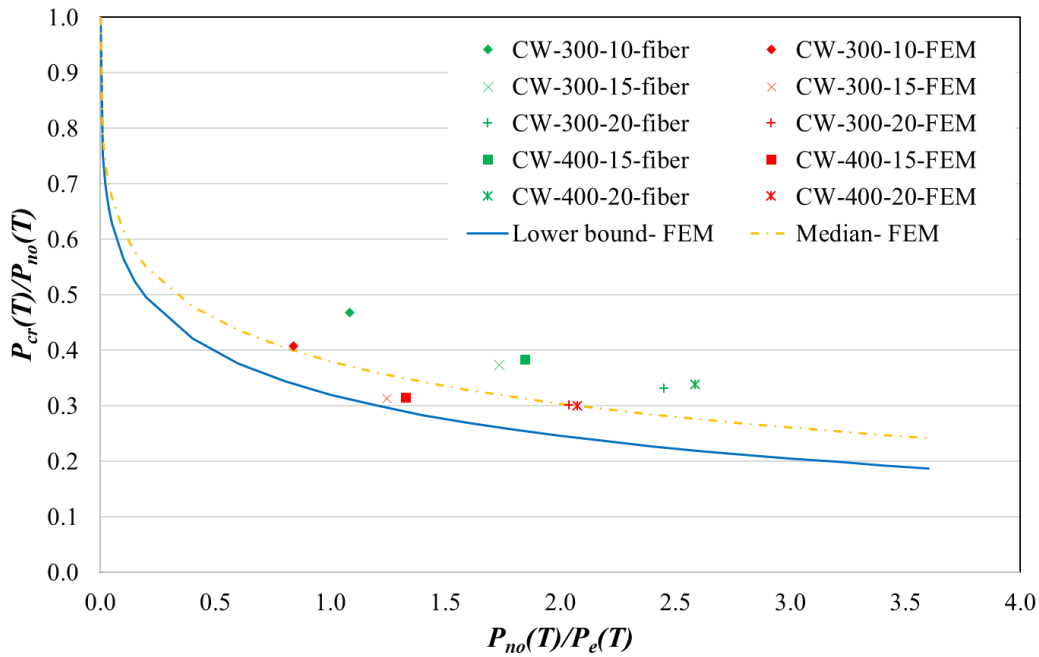


(b)

Figure 5.7: Comparison of axial displacements for (a) CW-200 specimens and (b) CW-300 specimens using strip method



(a)



(b)

Figure 5.8: Normalized results of the comparison between fiber-model and FEM data for (a) CW-200 specimens and (b) CW-300 & CW-400 specimens using strip method

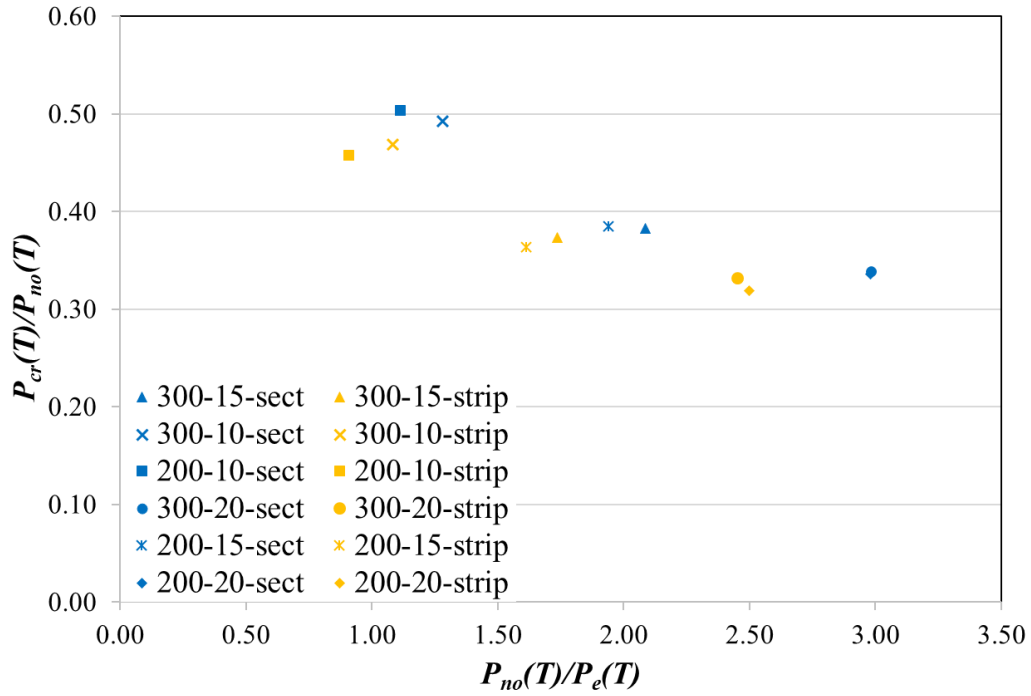


Figure 5.9: Comparison of normalized load vs slenderness data for section method and strip method for fiber-model

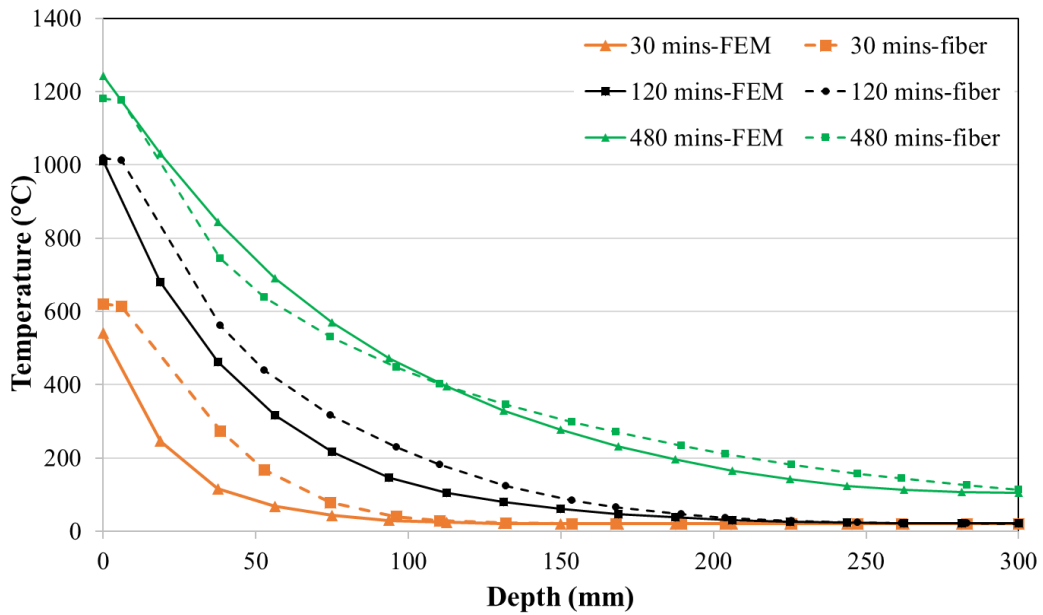


Figure 5.10: Comparison of cross-section temperature profiles at three time instants (CW-300) for fiber model and FEM for single-sided heating

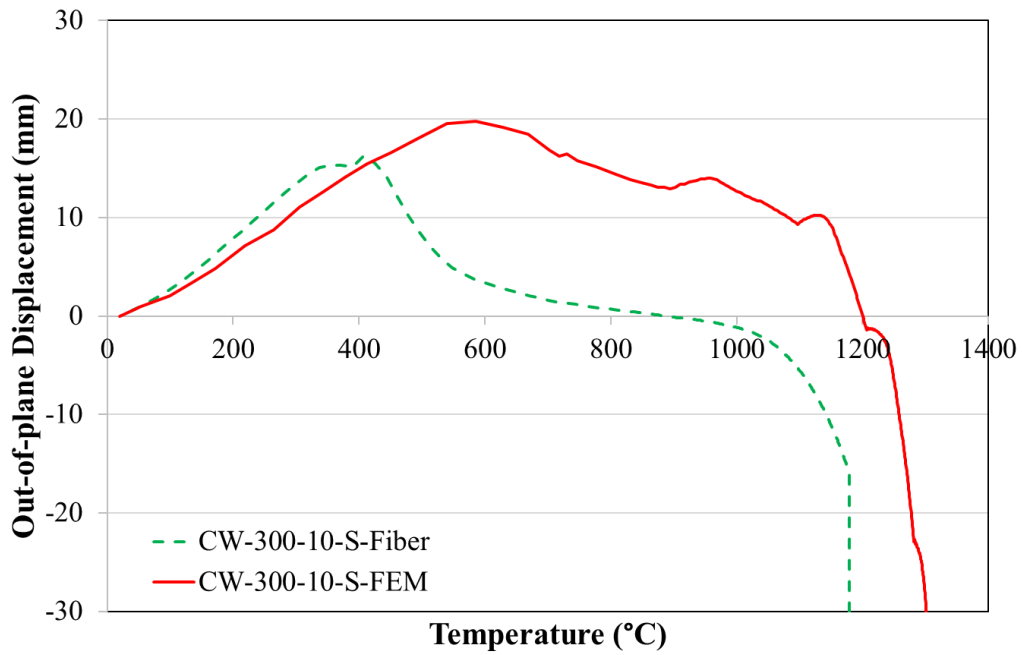


Figure 5.11: Comparison of fiber model and FE analysis predicted out-of-plane displacement against temperature for single-sided heating of the exposed steel surface for CW-300-10 specimen

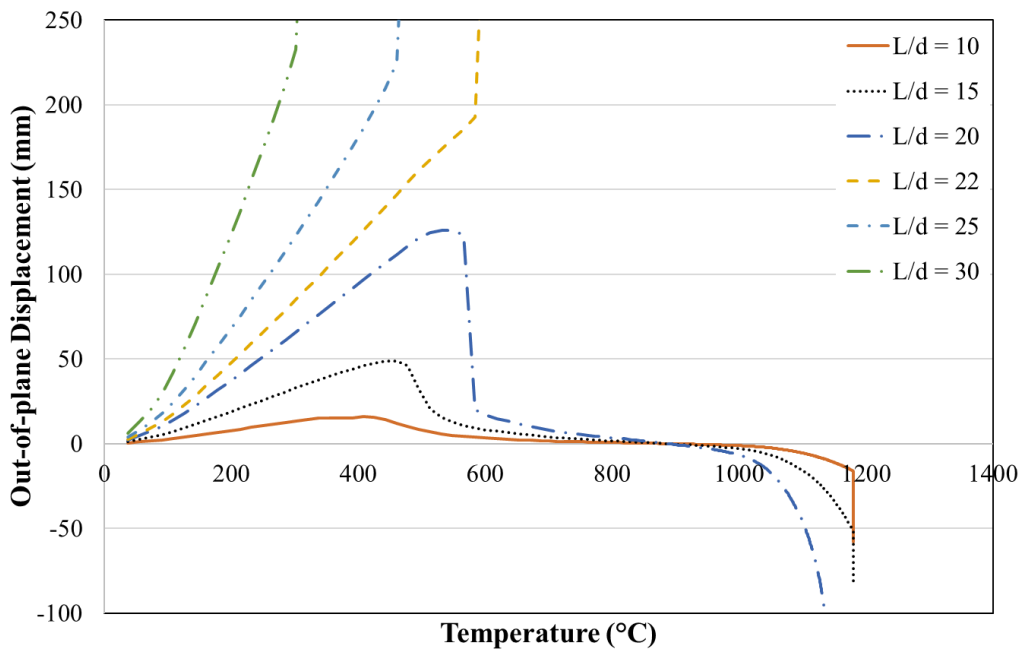


Figure 5.12: Out-of-plane displacement against temperature of the exposed steel surface for 6 slenderness (L/d) ratios for CW-300-xx-20 wall section for single-sided heating

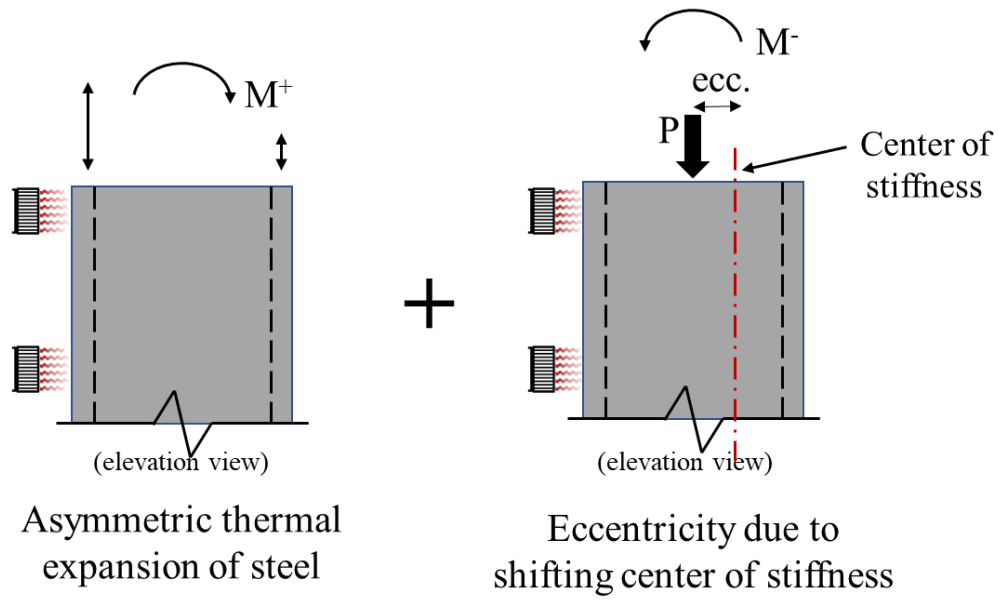
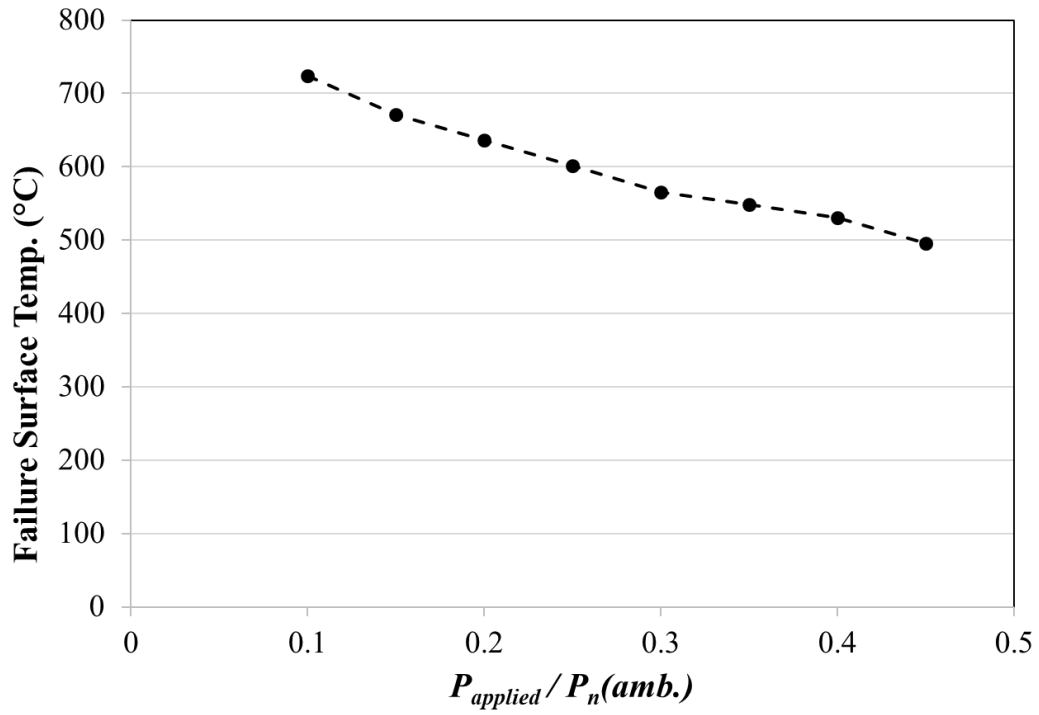
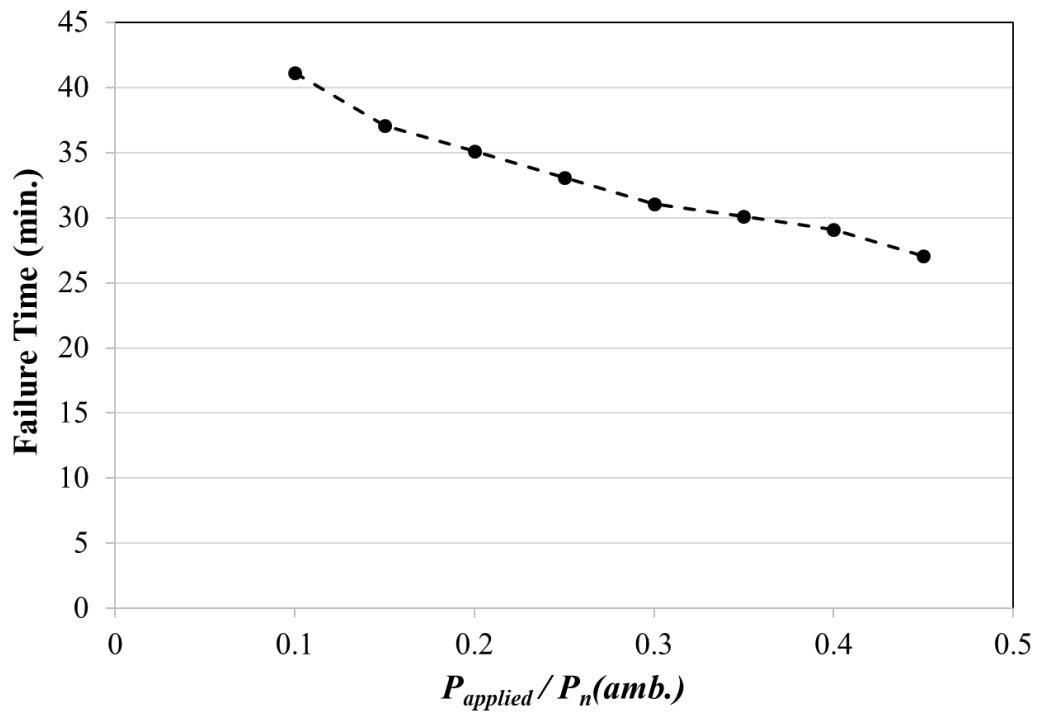


Figure 5.13: Representation of the two types of moments generated in a wall section exposed to asymmetric heating



(a)



(b)

Figure 5.14: (a) Failure surface temperature and (b) Failure time vs applied axial load ratio for slenderness = 25 (CW-300-25) for single-sided heating

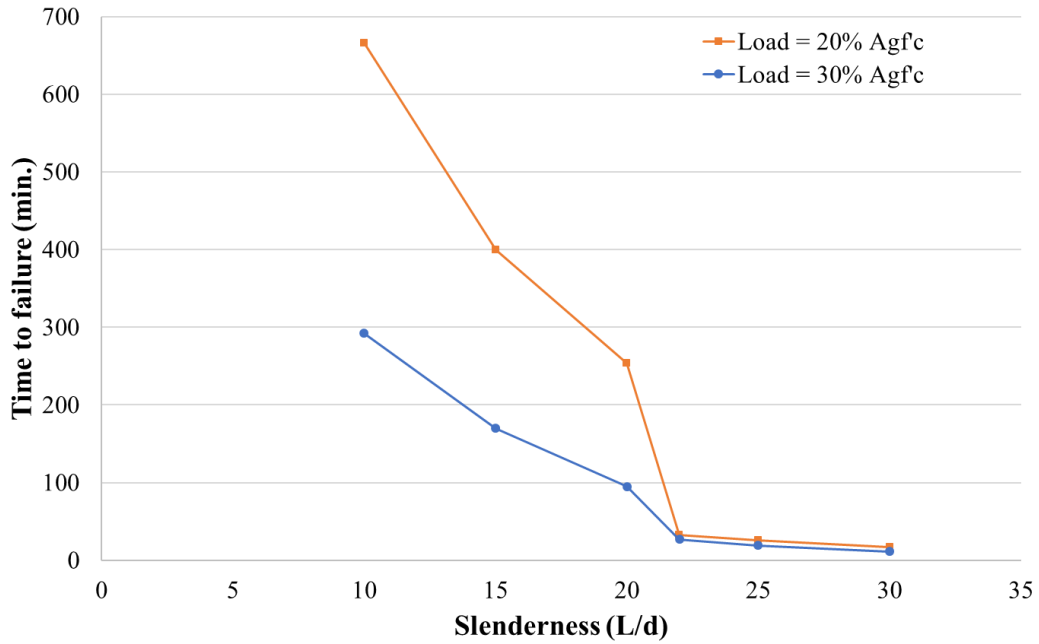


Figure 5.15: Variation of time to failure (fire resistance) with wall slenderness (single-sided heating) for applied axial load equal to 20% and 30%  $A_g f_c$  for CW-300 specimens

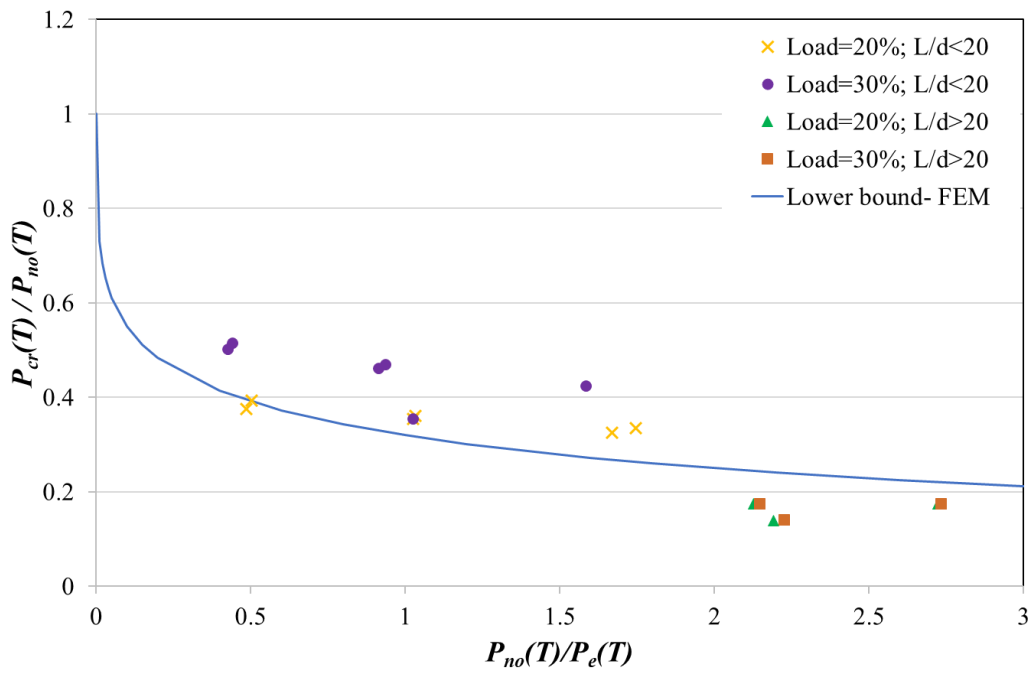


Figure 5.16: Normalized critical load vs slenderness data points for single-sided heating

## 6. SUMMARY AND CONCLUSIONS

This thesis presents a study of strength and stability behavior of composite axial members at elevated temperatures. For this purpose, a cross-section based 2D fiber model was developed to simulate composite axial members under fire loading. This model incorporated algorithms of heat transfer, calculation of moment-curvature response and inelastic buckling. The fiber model was validated at ambient and elevated temperatures using experimental data and 3D FE results. Multiple time-temperature curves, material models and heating scenarios were programmed to provide the flexibility of analysis. A graphical user interface was developed for the fiber model, that would allow the user better interaction with the model. The user interface allows the fiber model to be run as an analysis or design tool, and provides various options to visualize the results.

Using this fiber model, the effect of various parameters on the stability of CFTs under uniform fire loading was investigated. A capacity equation for CFTs at elevated temperatures was also developed and proposed. C-PSWs/CF were modeled using the fiber model and the results compared to FE analysis. Fiber model results were also compared against the proposed capacity equations for C-PSWs. Two modeling techniques of C-PSWs were explored: the section-based approach and the strip-based approach. Single-sided heating of C-PSWs was also modeled and studied using the strip-based approach.

Results of the parametric study on CFTs indicated that various parameters have differing effects on column behavior. Concrete compressive strength and section slenderness have a significant influence on the capacity of CFTs. Load capacity of CFTs was seen to decrease with decreasing concrete strength and increasing cross section slenderness. However, steel yield strength and aspect ratio had a minor effect on the load capacity. Also, it was observed that column capacity was nearly independent of all the four parameters at high temperatures ( $\sim 900^{\circ}\text{C}$ ).

A layer of fire protection was seen to significantly increase the fire resistance (time to failure) of CFTs by restricting steel temperatures to  $\sim 700^{\circ}\text{C}$ . However, for a given steel surface temperature, columns with fire protection had a lower axial load capacity due to a higher average concrete temperature. Design equations were proposed to calculate the capacity of CFTs at elevated temperatures. A lower bound, a median, and a simplified bi-linear equation were proposed based on the parametric study results.

C-PSW/CF specimens modeled using the two approaches gave results consistent with FE analysis and the proposed capacity equations. The strip-based approach was seen to be more consistent with FE models and more conservative as it neglected the additional strength due to wall boundary elements. It was hence recommended to use the strip-based approach for modeling C-PSW specimens. Single-sided heating of walls was modeled and studied using the strip-based approach. It was observed that walls with slenderness greater than 20 have low fire resistance to asymmetric heating, irrespective of the applied axial load. This is due to moments resulting from the asymmetric temperature gradient. Walls with slenderness less than 20 have a significantly higher fire resistance, with specimens remaining stable up to 600 minutes. Additionally, the proposed capacity equations for C-PSWs were seen to be adequate for walls with slenderness less than 20 exposed to asymmetric fire loading. It was recommended based on these observations to define slenderness limits for walls that would be exposed to asymmetric heating.

From the results, it can be concluded that the 2D fiber model is a viable alternative to 3D finite-element models for analyzing composite axial members. It was developed to be applicable to a wide range of members and heating scenarios and was seen to give accurate results. The limiting assumptions made in the development of the fiber model can be further minimized through additional research and development, which would expand the scope of applicability of the model.

As future work, a study to develop equations for predicting fire resistance (time to failure) of composite axial members is recommended. A detailed parametric study (similar to the study on CFTs) is recommended for C-PSWs exposed to asymmetric fire loading, to better characterize the effect of various parameters. Detailed studies are also recommended to specify limits on slenderness and the applied axial load for asymmetric fire conditions. Similar studies can also be performed for CFTs exposed to asymmetric fire loading (one-sided or three-sided heating) and design equations developed for the same.

## REFERENCES

- [1] AISC (American Institute of Steel Construction). (2016). "Specification for Structural Steel Buildings", 15th Edition, AISC 360, Chicago, IL
- [2] ASTM (American Standards of Testing and Materials). (2003). "Standard Test Methods for Fire Tests of Building Construction and Materials", ASTM E119, West Conshohocken, PA
- [3] Bhardwaj, S. R., Varma, A. H., & Wazalwar, P. (2019a). "Axial force-biaxial moment-vector shear (P-M-V) interaction for steel-plate composite (SC) wall piers". *Nuclear Engineering and Design*, 349, 162–173. <https://doi.org/10.1016/j.nucengdes.2019.04.022>
- [4] Bhardwaj, S.R., Sharma, S., Taghipour Anvari, A. and Varma, A.H. (2019b). "On the Stability of Composite Plate Shear Walls under Fire Loading." *Proceedings of the Annual Stability Conference-Structural Stability Research Council*, St. Louis, MO, April 2-5, 2019
- [5] Eurocode 4. (2005). "Design of composite steel and concrete structures- Part 1-2: General rules - Structural fire design", EN 1994-1-2, Brussels, Belgium.
- [6] Fischer, E.C., and Varma, A.H. (2017). "Fire Resilience of Composite Beams with Simple Connections: Parametric Studies and Design." *Journal of Constructional Steel Research* 128, 119–135. <https://doi.org/10.1016/j.jcsr.2016.08.004>.
- [7] Heinisuo, M. and Jokinen, T. (2014). "Tubular Composite Columns in a Non-Symmetrical Fire." *Magazine of Civil Engineering* 49 (5): 107–120. <https://doi.org/10.5862/MCE.49.11>.
- [8] Hong, S. (2007). "Fundamental Behavior and Stability of CFT Columns Under Fire Loading", Purdue University
- [9] Hong, S., Varma, A. H., 2008. "Analytical modeling of the standard fire behavior of loaded CFT columns", *Journal of Constructional Steel Research*, 65, 54-69. <https://doi.org/10.1016/j.jcsr.2008.04.008>
- [10] Hong, S. and Varma, A. H. (2009). "Predicting Fire Behavior of Composite CFT Columns Using Fundamental Section Behavior". *Journal of ASTM International*, 7 (1), 1-23. <https://doi.org/10.1520/JAI102311>

- [11] Kodur, V.K.R., Mackinnon, D.H. (2000). “Design of Concrete-Filled Hollow Structural Steel Columns for Fire Endurance.” *Engineering Journal - American Institute of Steel Construction* 37 (1): 13–24.
- [12] Lai, Z., Varma, A.H. (2016). “Effective Stress-Strain Relationships for Analysis of Non-compact and Slender Filled Composite (CFT) Members”, *Engineering Structures*, 124, 457-472. <https://doi.org/10.1016/j.engstruct.2016.06.028>
- [13] Lie, T., ed. (1992). “Structural Fire Protection” *Manual and Reports on Engineering Practice No. 78*, ASCE, New York, N.Y.
- [14] Lie, T.T. and Irwin, R.J. (1995). “Fire Resistance of Rectangular Steel Columns Filled with Bar-Reinforced Concrete,” *Journal of Structural Engineering*, Vol. 121, No. 5, 797–805. [https://doi.org/10.1061/\(ASCE\)0733-9445\(1995\)121:5\(797\)](https://doi.org/10.1061/(ASCE)0733-9445(1995)121:5(797))
- [15] Lue, D. M., Liu, J.-L., and Yen, T. (2007). “Experimental study on rectangular CFT columns with high-strength concrete”, *Journal of Constructional Steel Research*, 63, Issue 1, 37–44. <https://doi.org/10.1016/j.jcsr.2006.03.007>
- [16] MathWorks (2019). MATLAB R2019b Documentation, The MathWorks Inc., Natick, MA
- [17] Poh, K.W. (2001). “Stress-Strain-Temperature Relationship for Structural Steel”, *Journal of Materials in Civil Engineering*, Vol. 13, 371-379. [https://doi.org/10.1061/\(ASCE\)0899-1561\(2001\)13:5\(371\)](https://doi.org/10.1061/(ASCE)0899-1561(2001)13:5(371))
- [18] Simulia (2016). ABAQUS 2017 Documentation, Dassault Systemes Simulia Corporation Providence, RI
- [19] Taghipour Anvari, A., Bhardwaj, S.R., Wazalwar, P. and Varma, A.H. (2020a). “Stability of SpeedCore Walls under Fire Loading: Summary of Numerical Analyses”, *Proceedings of the Annual Stability Conference*, Structural Stability Research Council, Atlanta, Georgia, April 21-24, 2020
- [20] Taghipour Anvari, A., Bhardwaj, S.R., Wazalwar, P., Varma, A.H. (2020b). “Performance-Based Structural Fire Engineering of Buildings with Concrete-Filled Composite Plate Shear Walls (C-PSW/CF)” Final Report, Purdue University, West Lafayette, IN

- [21] Wazalwar, P., Bhardwaj, S.R., Taghipour Anvari, A., Varma, A.H. (2020). “Stability of Composite Axial Members Under Fire Loading. ”, *Proceedings of the Annual Stability Conference*, Structural Stability Research Council Atlanta, Georgia, April 21-24, 2020